Investigation of the dynamic properties of additively manufactured thin walled structures

used for hydro elastic experiments

MT-MEP

V.W.S. van Troost

Delft University of Technology

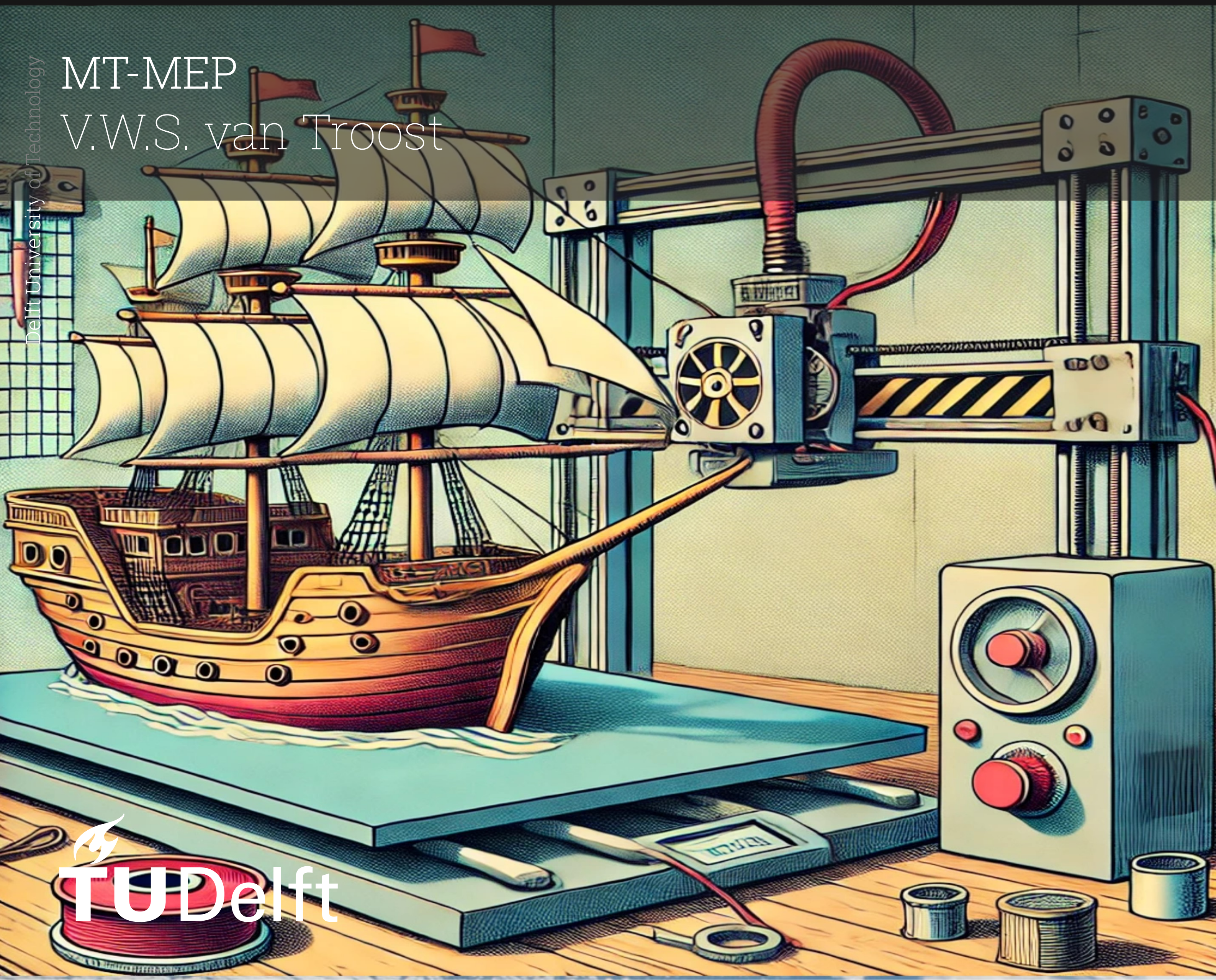

Investigation of the dynamic properties of additively manufactured thin walled structures

used for hydro elastic experiments

by

V.W.S. van Troost

Student Name	Student Number
Valentijn	5085101

Instructor: Dr. A. Grammatikopoulos
Project Duration: November, 2023 - November, 2024
Faculty: Faculty of Mechanical Engineering

Cover: OpenAI, ”Ship emerging from a 3D printer,” Generated by Chat-GPT, Oct. 2024.
Style: TU Delft Report Style, with modifications by Daan Zwaneveld

TU Delft

Thesis for the degree of MSc in Marine Technology in the specialization of *ship and offshore structure*

Investigation of the dynamic properties of additively manufactured thin walled structures

By

Valentijn W.S. van troost

Performed at

TU-Delft

This thesis MT.24/45.020.M is classified as confidential in accordance with the general conditions for projects performed by the TUDelft.

3 – 12 – 2024

Company supervisors

-

Thesis exam committee

Chair/Responsible Professor: Dr. A. Grammatikopoulos

Staff Member: MSc A.C. Azevedo Vasconcelos

Staff Member: Dr. J. Jovanova

Author Details

Studynumber:5085101

Preface

Preface

This document is the thesis for the Master's end project in Maritime Engineering: **Influence of Orthotropic Material Properties on Additively Manufactured Structures**. The research for this thesis was conducted at Delft University of Technology by a single master's student during the academic years 2023 and 2024. The research topic was provided by Dr. A. Grammatikopoulos, who aimed to investigate a possible explanation for the discrepancy found in an earlier thesis, that aimed to develop a 3D printed elastic model. This report describes the process of determining the orthotropic material properties of 3D-printed PETG and their degree of influence on the dynamic response of a scale model catamaran.

It is expected that the reader has basic knowledge of the maritime industry and the terms used with additive manufacturing. Readers that wish to know about the determination of the material properties can find this in chapter 1. Chapter 2 shows how the isotropic numerical model was modified to account for the measure material values and finally chapter 3 shows the impact of these values upon the structure.

I would like to express my gratitude to my supervisor Dr. A. Grammatikopoulos for providing this project and for always being available for support.

Valentijn van Troost - 5085101
Delft, November 2024

Summary

The objective of this research was to address how the material properties that appear in additively manufactured structures influence the behaviour of a fully elastic model that is produced with a 3D printer. and What considerations for the design can be made to reduce the influence. This investigation focused on the orthotropic and frequency-dependent behaviour of 3D-printed PETG material, along with the impact of a watertight epoxy layer on the outside of the model which is required to prevent water ingress.

To explore these aspects, test specimens were printed in all three principal printing directions and tested using a shaker setup. The specimens were specifically designed to evaluate both torsional and bending responses; they were thin-walled and designed to be arranged in consecutive sections suitable for 3D printing. Two testing configurations were employed: a weighted setup to lower the minimum measurable frequency range, and an unweighted setup to measure shear moduli. However, results from the weighted setup presented an issue where the eigenfrequencies from the second mode onward were higher than in the unweighted test. Consequently, Young's modulus values from the unweighted shear setup, which had their own errors with a negative viscous component, were used for further analyses.

These material properties were then incorporated into the numerical model, which was divided into four different material models. Laminate theory was applied to bulkheads and other transverse structures to predict the behaviour of horizontally printed sections, with the exception of the rear bulkhead, which had an additional epoxy layer. An orthotropic material model was applied to the longitudinal walls, including the deck and side walls. While the outermost skins combined orthotropic properties with an epoxy coating. Additionally, a Boundary element method was used to assess the effect of the water surrounding the model, generating an added mass matrix and hydrodynamic stiffness effects.

The updated model allowed for the assessment of each material property's influence on the dynamic response. The orthotropic behaviour was examined by varying the degree of orthotropic behaviour in relation to the base values of the vertical Young's modulus. For the epoxy comparison, the numerical model was run with and without the epoxy layer. Frequency dependency was evaluated through multiple manual iterations until convergence of the frequency.

Results indicated that among the three orthotropic Young's moduli, E1 consistently impacted eigenfrequencies, largely due to its effect on transverse stiffness in both bulkheads and plating. E3 only became relevant in the fourth mode, which is dominated by a two-point bending of the right pontoon. The inclusion of the epoxy layer increased the eigenfrequencies by 2.6% across the mode shapes, which is attributed to the added stiffness of the outer skin. Frequency dependency was not found to be significant for the first four frequencies, with only a 0.22 Hz variation across these eigenfrequencies.

To address the influence of the epoxy layer, it is recommended to reduce the epoxy thickness by applying thinner layers or investigating if the structure can be made waterproof by melting the outer surface thought or chemical process. The orthotropic behaviour may be harder to address; however, a combination of printing settings that yields a more isotropic result could be pursued. Alternatively, E1 could be used as the primary Young's modulus for model scaling to improve dynamic response alignment.

Contents

Nomenclature

Abbreviations

Abbreviation	Definition
FEM	Finite element model
FEA	Finite element analyse
CFD	Computational fluid dynamics
CMIF	Complex modal indicator function
FDM	Fused deposition modelling
RVE	Representative volume element
FRF	Frequency response function
BEM	Boundary element method
MAC	Modal assurance criterion
CAD	Computer-aided design

Symbols

Symbol	Definition	Unit
A	Area	[m^2]
B	Ship width	[m]
D	Draft	[m]
E	Elastic modulus	[Pa]
F	Force	[N]
G	Shear modulus	[Pa]
g	Gravitational constant Earth	[m/s^2]
H	Ship height	[m]
I	Area moment	[m^4]
J	Polar area moment	[m^4]
L	Ship length/beam length	[m]
L_{wl}	Length waterline	[m]
M	Mass/Moment	[kg]/[N/m]
T	Thickness	[m]
u	Ship speed	[m/s]
V	Velocity/shear	[m/s]/[N]
ω	Eigenfrequency	[rad/s]/[Hz]
λ	Scaling factor/wavelength	[-]/[m]
ν	Poisson ratio	-
ρ	Density	[kg/m^3]

1
Introduction

Additive manufacturing is a production method that builds up multiple layers of material. Following a CAD design that is prepared in advance. This production method can also be used within the maritime industry, as additive manufacturing has already been used to construct full scaled ships[1]. More interesting for maritime research, it has the capability to create fully flexible models as shown by the work of A. Keser [2]. However the choice of 3D printed materials is not without consequence as there are some material properties present within 3D printed structures that can influence the behaviour of elastic models. Which require additional consideration when one wants to use this method of production for these models.

1.1. Literary background

The use of models to predict the behaviour of full-scale ships dates back to 1872, when William Froude built the first basin for testing. These tanks have been instrumental in predicting the hydrodynamic interactions of ships, encompassing aspects such as resistance, propulsion, maneuverability, seakeeping, and structural response [3]. Thanks to advances in computational power within the computer industry, it has also become possible to determine most of these values using CFD programs. However, due to the excessive computational cost of CFD tools, they are still reserved for niche applications rather than wide engineering applications. This means experimental methods are still essential [4]. While most experimental results can be gained using simpler, rigid models, predicting or validating structural responses often requires flexible models.

Flexible models can realistically deform under fluid excitation with near-identical strains in both model and full-scale. This is achieved through three possible methods. The first involves joining multiple segments of the model via an elastic backbone scaled to have the same bending properties [5]. The second method joins ship segments via a series of flexible joints [6]. The final method, and the one we are most interested in, employs a fully elastic model which captures the full deformation of all structural elements [4]. The first two types are mainly used to measure longitudinal response but fall short when investigating higher frequencies dominated by non-longitudinal bending modes. Fully elastic models can account for these higher frequencies, but their presence in literature is limited due to design and production difficulties [2].

Advances in additive manufacturing now make it possible to produce structures with sufficient internal detail to include the influence of shear and transverse components, without the high costs associated with other production methods [7]. This production method can thus be used to create fully flexible models, as demonstrated by [2] and [8]. However, it also introduces certain dynamic material properties that must be accounted for. To properly scale the thickness of the structure, the Young's modulus needs to be determined. The Young's modulus of 3D-printed materials is influenced by many factors, one being that 3D-printed structures are orthotropic, requiring different thicknesses in each direction for proper scaling. Additionally, the Young's modulus of these materials is strain-rate dependent, meaning that wall thickness must also vary depending on the frequency range of interest. This variability makes finding an appropriate scaling factor challenging [3].

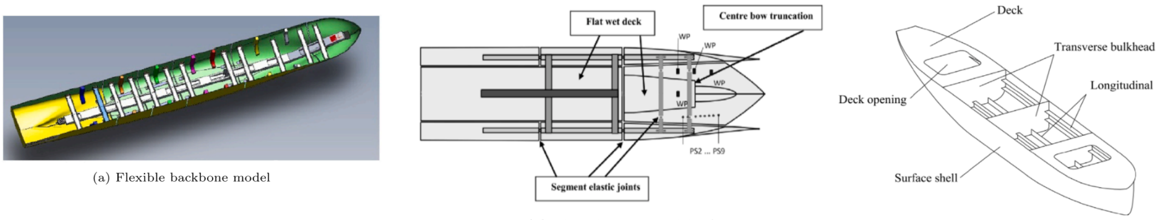

(a) Flexible backbone model

(b) Flexible joint model

(c) Elastic model

Figure 1.1: Different types of elastic models [3]

1.2. Properties additive manufacturing

Considerable research has already been conducted to determine the material characteristics of 3D-printed materials and the effects of different printing settings. S.H. Ahn et al.[9] Looks qualitatively at the influence of different printing settings on the ultimate tensile strength (UTS). These consist of Air-Gap/infill-ratio, raster angle, bead width, print temp, and colour. From which only the first two seem to have an impact on the ultimate tensile strength. O.A. Mohamed et all.[10] works with a regression model to look at the influence of layer thickness, air gap, raster angle, build orientation, bead width and numbers of contours on the complex modulus and dynamic viscosity of the material instead of just the static value. It finds that the air gap and number of contours have the largest impact. While J.L.C. Quintana et al.[11] looks at the effect of frequency, strain and raster angle on the complex Young's modulus, they show how at higher frequencies the material seems to harden as shown in figure 1.2. J. Chacón et all.[12] looks at the effect of build orientation and layer thickness on the static Young's modulus and UTS. M. Somireddy et al.[13] looks at the effect of layup and layer thickness on the static flexural stiffness and flexural strength. Y.H. Huang et al.[14] looked into the effect of layer height. But more importantly, they looked into the effect of different testing planes on the specimen, where they found the difference to be negligible. This resulted in a reduction in the types of specimens needed from 6 to 3. These specimens were then tested for their eigenfrequencies and successfully used to determine the 9 material properties. These results can be used to reduce the amount of experiments required.

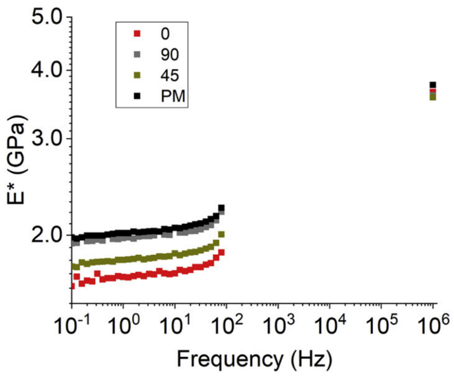

Figure 1.2: Complex Young's modulus from 3d Printed structures [11]

Continuing on A. Milovanović et al.[15] looked qualitatively at the influence of layer height, infill density and raster orientation for PP printing material. They also find that air-Gap/infill ratio seems to have the largest impact. Meanwhile P. Biswas et al. [16] worked on predicting the effect of different printing parameters upon the degree of an-isotropic behaviour. Using a representative volume element, they modeled the micro structure of 3d printed samples and compared the resulting material behaviour. They also did a parametric study upon layer height, filament width, and bond width. It was found that the porosity, which was created as off the result of the changes, influenced the orthotropic behaviour. Similarly L. Sosa-Vivas et al[17] looked into the effect of printing parameters on the elastic modulus in both directions in the printing plane. They found that printing speed doesn't effect the degree of orthotropic behaviour or the density. Additionally they suggest a relationship between the two factors.

Some studies focus on models predicting the elastic behaviour in any direction of 3D printed specimens based on nine engineering constants. Consisting of Young's moduli, Poisson ratio's and shear moduli. The initial work seems to have been done by J.F. Rodrguez et al[18]. These Moduli are all added to a stiffness matrix and used to calculate the stresses from the strain, measured in experiments. R. Zou et al [19] gave a simplified linear relationship between raster angle and ultimate strength, while modelling the specimens as transversely orthotropic material. T. Yao et al[20] shows that the Tsai-Hill anisotropic yield criterion can be used to determine ultimate tensile strength (UTS) for any angle, while also measuring the effect of layer thickness on the UTS. The resulting line is seen to agree better than the linear relationship of R. Zou et al[19]. T. Yao et al[21]'s work is similar but includes the third dimension allowing for prediction of mechanical properties in any arbitrary direction. Both of these combined show that the isotropic material theory of I.M. Daniel et al [22] can be applied to 3D printed structures to predict mechanical properties. This also gives a model for the horizontal parts of 3d printed structures which can be treated as composite materials. This saves time and samples as only the principle Young moduli need to be determined.

Finally, some papers investigate finite element analysis(FEA) of 3D printed structures to predict static and dynamic behaviour. M. Domingo et al [23] looked into the static response of a simple printed structures. They found that when given the full stiffness matrix the FEA could predict within 7.3% deviation the response of the structure. S. Jiang et al [24] used FEA to predict the vibration response of a 3d printed laminated specimen, showing a discrepancy of around 0.63% to 1.75% for the eigenfrequencies.

From the above research, two main gaps were identified to be the focus of my MEP. Firstly, while there is significant knowledge about the degree to which 3D-printed material is orthotropic and has a strain rate-dependent elastic modulus, there is a lack of understanding regarding how these material properties impact the dynamic response, particularly in structures resembling the internals of a ship. Secondly, although much research has been conducted on the material properties, including ultimate failure strength, it has primarily focused on specific materials with printer settings that differ from those we are using. As a result, the findings from previous studies cannot be directly applied to our research, leaving us with no clear understanding of these properties in our own material, therefore requiring us to determine them for our own.

1.3. Proposed research

The aim of this research is to characterise the impact of selecting additive manufacturing as the production method for creating a fully elastic ship model. The primary focus is on the material properties that influence the dynamic response of the ship model. But we will also look at the effect of the needed watertight layer on the outside of the models. Specifically, this study delves into examining the effects of orthotropic behaviour and frequency dependant properties in thinned wall structures. The research question is formulated as follows:

- *How do the dynamic properties of 3d printed structures effect the response of thin walled structures.*

This main research question will be further subdivided into the following sub-questions to create a structure with which we will answer the main question.

- What material properties present in 3d printed structures should be determined for the design of 3d printed structures subjected to dynamic loads?
  - What types of experiments need to be performed to obtain those properties?
  - At what frequency does the shift from static to dynamic modulus occur?
- Which FEM model should be used to predict the impact of the material properties?
  - How can we predict the behaviour of parts of the structure which are neither vertical nor horizontal?
- What variable will be used for the impact of the material properties?

1.4. Planning and structure

To answer the research question the project was divided into three parts. The design of the initial experiments and their specimens to determine the different material values of 3d printed thin walled structures. The modification and validation of a existing FEM model with a existing elastic model created by A. Keser [2], and finally this model will be used to determine the impact of different material variables. Appendix A show the planning that was used during the project.

For those interested in the determination of the material properties of the PETG filament, this information is provided in Chapter 2. Chapter 3 focuses on translating these material properties into those used in the FEM of the elastic model, along with the incorporation of the epoxy layer and the hydrodynamic effects of the surrounding water. Chapter 4 examines the impact of different degrees of orthotropic behaviour, the epoxy layer and frequency-dependent behaviour. Finally the report concludes with a possible measures that can be taken to reduce the effect of the found influence.

2
Material properties of 3D printed structures

In order to determine the impact of the dynamic behaviour of 3d printed structures, we will first characterize the degree to which these material properties are present. In this chapter we will be detailing which material properties need to be investigated, the design of the specimen that were used in the experiments and the experiments themselves. But first we will cover Froude scaling and why it is important to correctly determine the Young's modulus.

2.1. Material characteristics of Froude scaling

As stated before, models are often used to investigate the behaviour of larger structures, to validate theoretical or numerical models. This scaling can be as simple as taking any length dimension and applying the chosen scaling factor. However when working with ship models only linear scaling of length fails to account for forces such as wave resistance. So instead, when creating a model that is meant for the towing tank, Froude scaling is used. This is a scaling method that scales both the length dimension and time dimension based of the Froude number:

$$Fr = \frac{V_m}{\sqrt{g * L_{wl,m}}} = \frac{V_s}{\sqrt{g * L_{wl,s}}} \tag{2.1}$$

This scaling method results in the scaling factors in table 2.1 for length and time. This results in the correct scaling of wave Resistance created by the model. One aspect that the Froude scaling doesn't account for, in the scaling of the hydrodynamic forces, is the viscous resistance. In order to scale this aspect properly the Reynolds number should be used. This method of scaling isn't used because it requires having to test at a significantly higher speed.

For the design of a fully elastic model it require that not only the hydro dynamic properties are the same but also the global bending dynamics. This means that the Young's modulus, stiffness and mass of this model should also be scaled with Froude scaling. This means that if the area moment is scaled directly one would scale with the quadratic of the scaling factor. This would result in thicknesses so thin that it would be impossible to produce and if successfully produced the resulting structure would be to fragile to resist any force put upon it. Instead of scaling the area moment it is easier to scale the bending stiffness EI. The bending stiffness is scaled by a combination of the scaling factor of the Young's modulus and area moment resulting in a scaling factor of the 5th power. Therefore allowing the structure to retain a minimal thickness by scaling down the Young's modulus instead.

Using this method of scaling the bending stiffness A. keser [2] created a fully elastic model based on a offshore installation catamaran. This vessel was scaled with a factor of 180 resulting in the dimension seen in table 2.2.

Variable	Unit	Scale factor
Length	m	λ
Time	s	$\lambda^{0.5}$
Mass*	kg	λ^3
Speed	m/s	$\lambda^{0.5}$
Inertia	m^4	λ^4
Force	$kg\frac{m}{s^2}$	λ^3
Pressure	n/m^2 or Pa	λ
Frequency	$1/s$	$\lambda^{-0.5}$

Table 2.1: Froude scaling factor for different values. **only holds when the density ratio of the water equals 1[3]*

Item	Ship	Model
L	198 [m]	1100 [mm]
B	90 [m]	500 [mm]
H	26 [m]	144.4 [mm]
D	10.5 m	58.3[mm]
M	84603.5 [ton]	14.52[kg]

Table 2.2: Scaled dimensions of model[2]

The model consisted of three main parts: the main hull, the crane and the cargo. The size of each of these parts was to large to print them using a single print requiring them to be split up in smaller section that could be printed. The hull was split into three parts longitudinally and at each bulkhead transversely. The last part in the design of the model entailed adding additional weight as the density of the JPEG used for the production was significantly less then that of steel. The weights are placed in such a way that they provide the correct center of gravity and the dynamic response remains the same. The completed model can be seen in figure 2.1

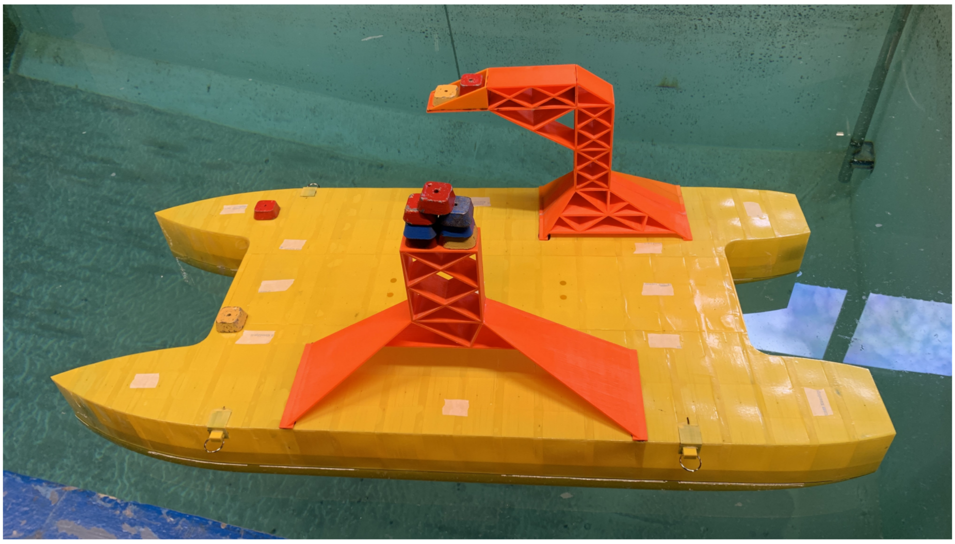

Figure 2.1: Completed model [2]

The model was designed with an isotropic Young's modulus of PETG with the value of $1.2e10^9$[Pa] and a Poisson ratio of 0.3887. However as stated before 3d printed structures aren't perfectly isotropic. They display orthotropic and frequency dependant behaviour. To see to what level these material behaviours would cause problems with Froude scaling, we first have to obtain the degree to which orthotropic behaviour and the frequency dependent behaviour are present.

2.2. Experiments

The degree of orthotropic behaviour and frequency dependency was determined through experimental analysis of 3d printed specimens. In order to fully define the behaviour, the experiment had to find the elastic properties in three directions. These direction are: longitudinal, transversal and vertical. These can also be revered to as the local x/y/z-directions, the coordinate system is shown in figure 2.2. These variables will allow for the construction of a complete stiffness matrix.

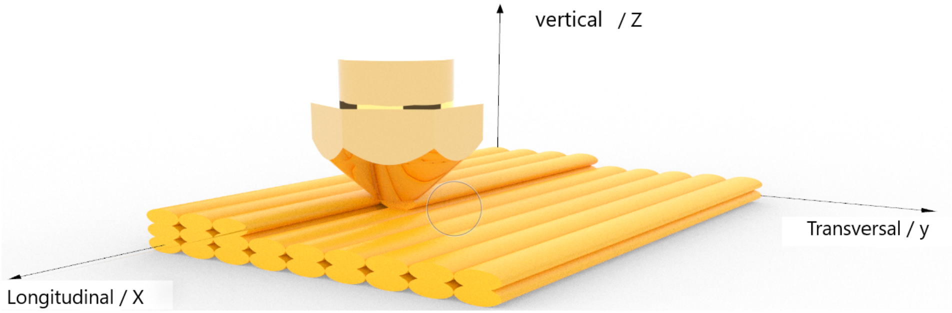

Figure 2.2: Local coordinate system of 3D printed material

2.2.1. Experimental theory

Flexural modulus

To find the flexural elastic modulus we will use the theory of free transversal vibration of beams as can be found in [25] and [26]. To determine the differential equation of the bending beam, we will look at a infinitesimally small slice of a beam which is located at (x). The slice is shown in figure 2.3. In this picture M is defined as the moment, V is shear force within the beam and F is the loading per unit length put on the beam.

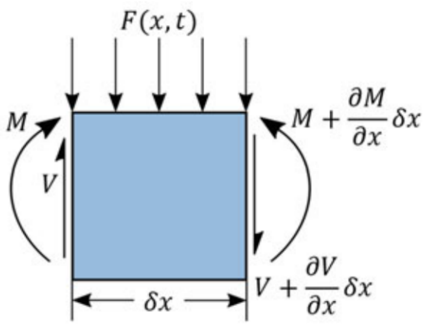

Figure 2.3: Moment and shear forces [25]

Using Newton's second law of motion, the sum of the moments around the block looks as follows.

$$F = ma$$
$$M + \frac{\delta M}{\delta x}\delta x - M - (V + \frac{\delta V}{\delta x}\delta x)\delta x - F(x,t)\delta x\frac{\delta x}{2} = \rho A \delta x \frac{\delta x}{2}\frac{\delta^2 v}{\delta t^2} \tag{2.2}$$

Two things should be noted when looking at this equation. Firstly the sum is taken around the left side and secondly the rotational inertia is neglected. By letting δx in equation 2.2 approach zero, the following relationship is created.

$$\frac{\delta M}{\delta x} = V \tag{2.3}$$

To gain the dynamic equilibrium for the transverse bending we also use newton's second law in the transversal direction. As shown in equation 2.4.

$$\rho A \delta x \frac{\delta^2 v}{\delta t^2} = V - V - \frac{\delta V}{\delta x}\delta x - F(x,t)\delta x \tag{2.4}$$

This equation is further refined by canceling out the shear forces and by applying 2.2 to the change of shear over the beam. The following equation is created.

$$\rho A \frac{\delta^2 v}{\delta t^2} = -\frac{\delta^2 M}{\delta x^2} - F(x,t) \tag{2.5}$$

Using the Euler Bernoulli theory, the bending moment can be expressed as a function of the vertical displacement. Resulting in equation 2.6.

$$M = EI \frac{\delta^2 v}{\delta x^2} \tag{2.6}$$

By putting 2.6 into 2.5 we get the following.

$$\rho A \frac{\delta^2 v}{\delta t^2} = -\frac{\delta^4 EIv}{\delta x^4} - F(x,t) \tag{2.7}$$

The beam in question is assumed to be free of any external forces which allows us to say F(x,t) =0. At the same time we can assume that E and I are constant for the length of the whole beam. Allowing us to rewrite 2.7 to:

$$\rho A \frac{\delta^2 v}{\delta t^2} = -EI \frac{\delta^4 v}{\delta x^4} \tag{2.8}$$

Which in turn can be expressed as

$$\frac{\delta^2 v}{\delta t^2} = -c^2 \frac{\delta^4 v}{\delta x^4} \tag{2.9}$$

with the constant C:

$$c = \sqrt{\frac{EI}{\rho A}} \tag{2.10}$$

Equation 2.9 is a fourth order differential equation, in order to solve it we use variable separation. Thereby splitting it in the time dependant part and the space dependant part.

$$v = \phi(x)\psi(t) \tag{2.11}$$

Substituting this into 2.9 obtains the following:

$$\phi(x)\frac{\delta^2 \psi(t)}{\delta t^2} = -c^2 \frac{\delta^4 \phi(x)}{\delta x^4}\psi(t) -> \phi(x)\psi"(t) = -c^2 \phi(x)^{''''}\psi(t) \tag{2.12}$$

By assuming a sinusoidal function within the time dependency, we can define the constant ω as follows.

$$\frac{\psi"(t)}{\psi(t)} = -c^2 \frac{\phi(x)^{''''}}{\phi(x)} = -\omega^2 \tag{2.13}$$

This allows us to separate the spacial en time terms along the following lines.

$$\psi"(t) + \omega^2\psi(t) = 0, \phi(x)^{''''} - (\frac{\omega^2}{c^2})\phi(x) = 0 \tag{2.14}$$

The time dependant equation is a simple second order equation, which means it can expressed as following:

$$\psi(t) = B_1 cos(\omega t) + B_2 sin(\omega t) \tag{2.15}$$

In order to solve the spacial dependant part of the equation, we assume that $\phi(x) = A_i e^{\lambda x}$ this creates the following series of equations with $\eta = \sqrt{\omega/c}$.

$$\begin{aligned} \phi(x)'''' - (\frac{\omega^2}{c^2})\phi(x) &= 0 \\ \lambda^4 A e^{\lambda x} - \frac{\omega^2}{c^2} A e^{\lambda x} &= 0 \\ (\lambda^4 - \eta^4) A e^{\lambda x} &= 0 \\ \lambda^4 - \eta^4 &= 0 \end{aligned} \tag{2.16}$$

There are four solutions to this equation, meaning that the spacial component of the solution looks as follows:

$$\phi(x) = A_1 e^{\eta x} + A_2 e^{-\eta x} + A_3 e^{i\eta x} + A_4 e^{-i\eta x} \tag{2.17}$$

Which in turn can be rewritten using Eulers complex notation to the following.

$$\phi(x) = A_5 cos(\eta x) + A_6 sin(\eta x) + A_7 cosh(\eta x) + A_8 sinh(\eta x) \tag{2.18}$$

Using these equation 2.12 yields.

$$v(x,t) = (B_1 cos(\omega t) + B_2 sin(\omega t))(A_5 cos(\eta x) + A_5 sin(\eta x) + A_5 cosh(\eta x) + A_5 cosh(\eta x)) \tag{2.19}$$

With the following eigenfrequencies.

$$\omega = \frac{(\eta L)_i^2}{L^2}\sqrt{\frac{EI}{\rho A}} \tag{2.20}$$

As can be seen in equation 2.20 the eigenfrequency is dependant upon the value of the constant ηL. This constant is in turn determined by the boundary condition on either end of the beam. These ends can be either free, pinned, clammed or possibly have a mass placed at the end. As it will later be used during the experiment we also include the derivation of the free-free condition. For a free-free beam the end condition consist of no moment or shear force at either end. This means that for x=0 and x=L equation 2.6 and 2.3 also equals 0.

$$\begin{aligned} \frac{\delta^2\phi(0)}{\delta x^2} = 0 &\rightarrow -A_5\eta^2 cos(0) - A_6\eta^2 sin(0) + A_7\eta^2 cosh(0) + A_8\eta^2 sinh(0) = 0 \\ \frac{\delta^2\phi(L)}{\delta x^2} = 0 &\rightarrow -A_5\eta^2 cos(\eta L) - A_6\eta^2 sin(\eta L) + A_7\eta^2 cosh(\eta L) + A_8\eta^2 sinh(\eta L) = 0 \\ \frac{\delta^3\phi(0)}{\delta x^3} = 0 &\rightarrow A_5\eta^3 sin(0) - A_6\eta^3 cos(0) + A_7\eta^3 sinh(0) + A_8\eta^3 cosh(0) = 0 \\ \frac{\delta^3\phi(L)}{\delta x^3} = 0 &\rightarrow A_5\eta^3 sin(\eta L) - A_6\eta^3 cos(\eta L) + A_7\eta^3 sinh(\eta L) + A_8\eta^3 cosh(\eta L) = 0 \end{aligned} \tag{2.21}$$

These equations yield the following:

$$\begin{aligned} -A_5 + A_7 &= 0 \\ -A_5 cos(\eta L) - A_6 sin(\eta L) + A_7 cosh(\eta L) + A_8 sinh(\eta L) &= 0 \\ -A_6 + A_8 &= 0 \\ A_5 sin(\eta L) - A_6 cos(\eta L) + A_7 sinh(\eta L) + A_8 cosh(\eta L) &= 0 \end{aligned} \tag{2.22}$$

These equation allow us to say that A_5 = A_7 and A_6 = A_8. leaving us with two equations.

$$\begin{aligned} A_5(-cos(\eta L) + cosh(\eta L)) + A_6(-sin(\eta L) + sinh(\eta L)) = 0 \\ A_5(sin(\eta L) + sinh(\eta L)) + A_6(-cos(\eta L) + cosh(\eta L)) = 0 \end{aligned} \tag{2.23}$$

In order for there to be non-trivial solutions to these equation the determinant should be zero. This result in the following value for η.

$$cos(\eta L)cosh(\eta L) = 1 \tag{2.24}$$

The equation has an infinite number of solutions each corresponding to a different eigenmode. One solution to highlight is the zero solution as it represents the rigid body motions, with increasing values representing higher modes. We are therefore able to link the elastic modulus to the eigenfrequencies.

Shear modulus

The flexural elastic modulus wasn't the only elastic value that we were interested in. The shear modulus can be found using the torsional vibration of beams. The method is largely the same beginning with a infinitesimally small slice of a beam with shear modulus G, density of ρ and an polar inertia of J at location x which can be seen in figure 2.4.

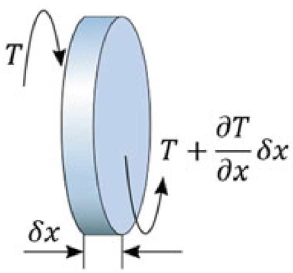

Figure 2.4: Moment and sheaf forces [25]

Using Newtons second lay we obtain the following equation for the dynamic behaviour for this free beam.

$$\rho J \frac{\delta^2 \theta}{\delta t^2}\delta x = T + \frac{\delta T}{\delta x}\delta x - T\delta x \tag{2.25}$$

Equation 2.25 is a second order differential equation which we can solve in the same method of variable separation as equation 2.12. This separation gives two second order differential equations which when solved, give the following equation for the spacial and time equation.

$$\phi(x) = A_1 cos(\frac{\omega x}{c}) + A_2 sin(\frac{\omega x}{c}), \psi(t) = B_1 cos(\omega t) + B_2 sin(\omega t) \tag{2.26}$$

For these equations the value of A_1, A_2, B_1, B_2 and ω are dependant on the boundary equation of the beam. Here we will also use a free-free condition to asses the shear modulus at different frequencies. The boundary equations for torsional bending become $T(0) = 0$ and $T(L) = 0$. With these two boundary equations 2.26 results in the following:

$$A_1 \frac{\omega}{c} sin(\frac{\omega L}{c}) = 0 \tag{2.27}$$

In order for there to be a non trivial solution the sinus term in the equation should be zero meaning the the eigenfrequency of the torsional bending is as follows. For n = 0,1,2,3,4,... with n=0 being the rigid body motion.

$$\omega = \frac{n\pi}{L}\sqrt{\frac{G}{\rho}} \tag{2.28}$$

However this method of calculating the bending and torsional eigenfrequency, assumes that the beam can be approximated as a Euler beam. One of the assumption of the Euler beam is that the cross section doesn't change due to bending. This causes a conflict with one of the design principles of the specimen that we wish to use later on to determine the different elastic moduli, namely that we want a thin walled structure. Which cause warping to become a contributor to bending. Instead of this equation a Fem, using shell elements, will be created to determine the different moduli.

The thin wall nature of the bending doesn't only cause warping which prevents a Euler beam assumption, it also causes us to measure different shear moduli at the same time. In the case of vertical specimen everything is fine as the method of printing results in the G_{OL} being measured along the length of the whole cross section. For the other two specimen types there is a combination of different shear moduli making up the elastic response. For the longitudinal specimen this consist of G_{LT} for the web and G_{LO} for the flanges of the cross section. This means that the G that is measured from the shaker testing is a combination of these two. In order to find the ratio to which these two are combined, we used Saint Venant theory, for torsion in open thin structures. This theory holds that total torsional stiffness of a cross section can be found by adding the torsional stiffness of each section separately where $GI_{tot} = \sum GI_{1,2,3}$. The Area moment in this formula is equal to $\alpha * b * t^3$ with α being equal to 1/3 for thickness ratios larger then 1/10 [27]. Due to the square nature of the specimen, the measured shear modulus for the longitudinal specimen is equal to $\frac{1}{3}G_{LT} + \frac{2}{3}G_{LO}$ and the measured modulus for the transversal specimen is $\frac{1}{3}G_{TL} + \frac{2}{3}G_{TO}$.

With the above mentioned relationships and the FEM we are able to determine the shear modulus as a function of frequency. This leaves one variable which we need to define the Stiffness matrix, the Poisson ratio's for each direction. As can be seen from the above theory the Poisson ratio can't be determined from the eigenfrequencies as the term doesn't appear anywhere within the derivation. Instead we have to determine the Poisson ratio's from the elastic properties. Thus equation 2.30 is used to calculate the poisson ratio, keeping in mind that it relies upon an isotropic assumption, no other option was seen as viable to find the Poisson ratios. Due to the symmetric nature of the stiffness matrix we only have to determine the value of half of the Poisson ration's, the other half can be found using the following equation.

$$\frac{\nu_{ij}}{E_i} = \frac{\nu_{ji}}{E_j} \tag{2.29}$$

The Poisson ratio's that will be used for the material model are the following $\nu_{xy}, \nu_{yz}, \nu_{xz}$. As these are the one's that are used by ANSYS mechanical as material characteristics. For isotropic materials the following equation is used to determine the Poisson ratio.

$$G = \frac{E}{2(\nu + 1)} \tag{2.30}$$

But in order to use this equation we must identify which E,G and ν are to be used together. For this the equation was changed to the following:

$$\begin{aligned} G_{ij} &= \frac{E_i}{2(\nu_{ij} + 1)} \\ \nu_{ij} &= \frac{E_i}{2G_{ij}} - 1 \end{aligned} \tag{2.31}$$

With these it was hoped to determine all Poisson's ratios and shear moduli but as will shortly be shown the measured shear moduli resulted in impossible values indicating a different method should be used. Direct measurement is highly advised

2.2.2. Specimen Design

When designing the test specimens that would be used for the determination of the different material values, we needed to keep several design rules in mind if we wanted the resulting values to be representative of those found in A. Keser's model. These design rules were as follows:

- **Thin-walled** - As previously mention we were interested in a thinned wall structure, because a normal 3D print usually consists of two distinct parts: the perimeters and the internal volume of the print. Perimeters, which circle around the internal volume, can be up to three or four lines thick and serve to improve the horizontal surface finish of the print and the resistance of the print to buckling. The internal volume consists of a zigzagging pattern that, depending on the infill percentage, fills the internal volume of the print, with larger percentages dramatically increasing the stiffness of any structure and the failure strength. As A. Keser's model was scaled down to wall thicknesses measured in millimetres, as such it mostly consists of perimeters. In order to create a similar structure, our specimen is designed to mimic this structure.
- **Torsion and bending** - The second aspect that we wish to include was to make a single specimen that could be used for both the shear modulus and the flexural modulus. This will decrease the required printing time, as a smaller amount of samples needs to be created and tested, the results in the total amount being nine instead of 18 for each direction.
- **Consecutive** - This requirement comes down to the limitation of the production method of additive manufacturing. A 3D printer is only capable of creating items of a certain scale dictated by the size of the printing bed and the height of the gantry on which the extruder is mounted. In the case of our 3D printer, it has a volume of 21x22x25 cm for length, width, and height. Using these small lengths increases the eigenfrequency of a beam as per 2.20 and 2.28. Which results in an expected eigenfrequency above the interested frequency range. To address the limited length of any sample, it was decided that by gluing multiple samples together, one could lower the frequencies. This does, however, require the individual sections to be attached to one another in a secure manner.
- **Printable** - Another limitation of the 3D printer is encountered with the presence of overhanging layers. This happens when the angle of any wall and the build plate are acute, causing the printer to place a line partially unsupported. Larger angles often don't cause issues, but angles of 40° or smaller can cause loose lines or lines that aren't melted together properly. Because of this, it was decided to avoid overhangs in the main direction of the testing specimen for each of the 3D testing directions.

With these design principles in mind, the following steps were followed in search of the final shape. Initially, a dog bone-type specimen was envisioned, as it was previously used in other research to determine the static elastic modulus [17]. While this shape did fit with some of the above-mentioned design rules, it was found lacking in others. The expected order of magnitude for the elastic and shear moduli indicated significant differences in eigenfrequencies, with bending being in the range of 0.001 Hz and torsional frequencies being in the range of 100 Hz. The second problem arose with the printing of the specimen in the Z-direction. This would require a print that consisted of a single wall. Previous experience with 3D printing and examples shown to us by Professor A. Grammatikopoulos, tells us that such a print has a high likelihood of vibration-induced defects in higher layers, or even the separation of the printed layers due to the limited cross-section in contact with the printing bed.

The next shape that was investigated consisted of a continuously square cross-section with a side length of around 1.0 cm. This continuous shape would allow for an increase in stability while printing and enhance bed adhesion. However, it was found that the bending frequency was still orders of magnitude larger than those of the torsional eigenfrequencies and that we would be unable to differentiate the different shear moduli. As this same design also didn't follow the thin-walled approach, it was quickly abandoned and replaced with a hollowed-out version. This lowered the expected frequencies to the desired range without requiring the sample to be meters in length.

The use of a hollowed-out section was seen as promising, so that design was iterated upon. In order to meet the consecutive criterion, it was decided to set the length of a single section to 20 cm and to place flat caps at the ends. This would add rigidity to the torsional bending and allow for easier attachment to one another. This design meets most of our criteria except that the vertical specimen would have a small overhang but it was decided to use support here as the overhang wasn't in the direction of testing. The final design can be seen in 2.5 with it dimension in table 2.3.

Length	Width	Height	Thickness	Mass
20 [cm]	1 [cm]	1 [cm]	0.8 [mm]	5.12 [g]

Table 2.3: Vibrational specimen as designed.

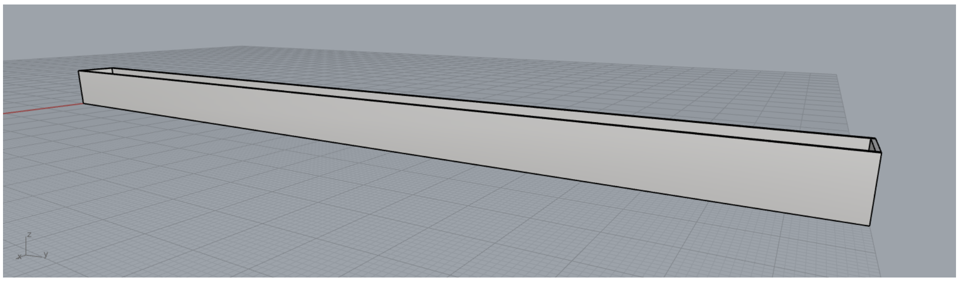

Figure 2.5: Individual piece of vibration beam

2.2.3. 3D printer settings

Because of the high amount of variable that can influence the material characteristic of 3d printed structure, [9–12, 28] we printed with the same parameters as those used by A. Keser [2]. This means that the following printing parameters were used in the production of specimens. Nozzle diameter is set 0.25 mm with a brass nozzle resulting in layers with a thickness around 0.28 mm. The Chosen filament is the eSUN PETG filament. In the previous study the filament was dried at 50°C to remove any moisture present in the roll due to long storage. The printing temperature was set of 230°C and the bed temperature to 80°C. Initial layer height was set to 0.15 mm with the following layer being set to 0.125 mm. Printing speed was set to 32 mm/s which is the same as the internal walls and bulkheads of the model. Any faster speed was found to cause skipping in the extrusion gears.

One of the produced transversal sample's can be seen in figure 2.6. upon inspecting the printed sample it was found that the most prevalent error was at the corners, these had bulging. It is suspected that this was caused by the lack of outer layers being present to hide this and the constant printer speed setting as the printer usually slows down for these corners. These bulges were removed with a scalpel to allow for the samples to be glue together. To check the accuracy of thicknesses produced by the printer a electronic caliper was used. Table 2.4 contains the measured dimensions of all three types of samples. The thickness of the sides was measured at 3 points for each side 1 cm from the ends and in the middle. Additionally all sample were weighed after they were joined together. This weight, together with the calculated volume resulted in a average density of the printed material of 1073.5 kg/m^3. This density is lower than the expected range of 1.270-1.380 [29]. This is likely due to the bulging of the outside and the presents of air between the layers lowering the measured density.

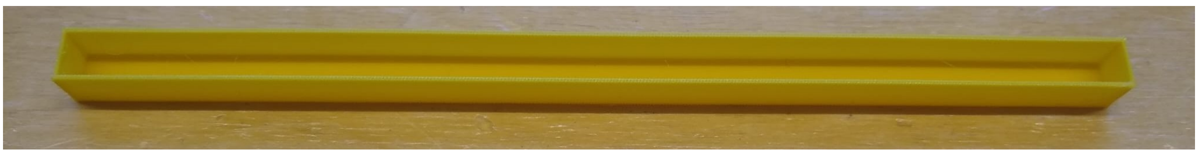

Figure 2.6: Individual specimen transversal direction

Specimen	Length	Width	Thickness	Volume(calculated)	Mass
Longitudinal-X	60.5± 0.4 [cm]	1.03$\pm$ 0.007[cm]	0.76 $\pm$0.02 [mm]	15.8 $[cm^3]$	15.8$\pm$ 0.08 [g]
Transversal-Y	59.86± 0.09 [cm]	1.05$\pm$ 0.01[cm]	0.90 $\pm$0.02 [mm]	16.1 $[cm^3]$	16.6$\pm$=0 [g]
Vertical-Z	61.1667± 0.23 [cm]	1.03$\pm$ 0.007[cm]	0.88 $\pm$0.03 [mm]	15.8 $[cm^3]$	16.53$\pm$0.33 [g]

Table 2.4: Measured dimensions test specimens

2.2.4. Experimental setup

Initially it was envisioned that a impact hammer would be used to determine the different eigenfrequencies of the specimens but after several attempts it was found that the specimen were too light and our experience with the impact hammer to little to produce usable results. With the specimens often jumping wildly or even breaking. Instead it was decided to make use of a modal shaker which was used by a fellow student who could explain the setup and workings. Using the modal shaker, two different setups were used for testing. A weighted approach for the flexural modulus and an un-weighted approach to find the shear modulus. However we will first go over the data acquisition system (DAQ) and equipment used as seen in 2.7 and 2.8 below.

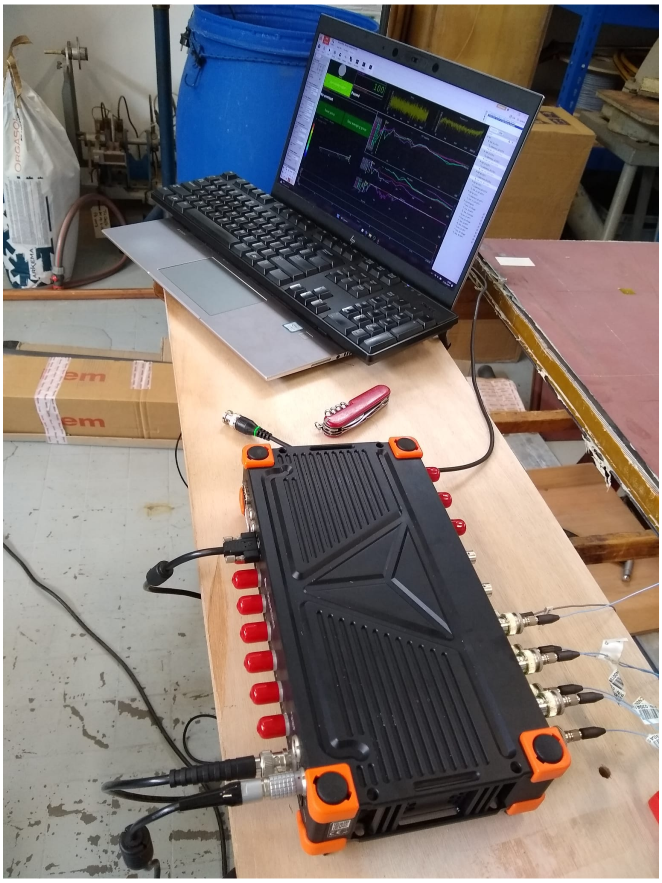

Figure 2.7: Sirius DAQ and laptop running DewesoftX

In the figure 2.7 two things are visible: A HP Z-book laptop running DewesoftX and a Dewesoft Sirius-HD-16xAcc Data Acquisition System. The latter is used to measure the voltages coming form the accelerometers and control the modal DS-MS-100 shaker, which excite the different specimens connected to it. The laptop is running DewesoftX 2024.2 which takes the measured results from the DAQ and determines the Frequencies Response Function (FRF) of the excitation.
DewesoftX also required the creation of a setup file which contained the different setting for the measurements. The acquisition range was set to 5000 Hz which gave a measured bandwidth of 2498 Hz. Next all sensors were set from Volt to IEPE and a 200$\pm$ mV measuring range was set, to avoid either overload or losing resolution. For the settings of the modal shaker, the excitation of the beam was set

to be a continuous random wave with a amplitude of 0.2V, resulting in a impact for of 0.3 N. With a signal overlap of 66.7%. The FRF was calculated with the average over a 100 hits with a resolution of .5 Hz. The shaker itself was attached 3 cm form the middle so the anti-symmetric modes would also be excited.

Figure 2.8: Setup weighted test

The first physical test setup can be seen in figure 2.8. Here one can see the joined specimens placed on top of two pieces of isolation foam placed 29 cm apart. This setup is used to approach a free-free condition. Initial for the hammer testing it was attempted to suspend the specimen from elastic bands but it was found that it was too light causing it to jump to the point that the strings were no longer in tension. For the modal shaker it was decided to place the specimen on foam and make sure it stayed in constant contact during the runtime to avoid any non-linear effect.

As stated two different setups would be used with the modal shaker to test for the eigenfrequencies of the material. For the weighted test 3 28.5 gram weights were attached to the specimen using double sided tape. This was done in order to lower the eigenfrequencies to below 10 Hz, as this was the lower end of the frequency band that we were interested in. In addition to these weights 11 1-directional PCB Piezotronics 352C22 accelerometers were used to measure the response of the beam to the excitation. They were placed in a even spacing along the length of the specimen, with the outer sensors being placed on top off the weights. As seen in 2.8.

The second test was meant to measure the shear modulus of the material. This method consisted of placing the shaker on one side of the specimen in such a way that it would cause a torsional moment in the beam, which would excite the torsional bending modes. In this case 10 accelerometers were placed along the length of the specimen in groups of 2, with them being placed side by side. This would allow for the identification of the torsional and bending modes of this setup.

In the figure we can also see the attachment point of the DS-MS-100 modal shaker on the left in the figure. This shaker is connected to the specimen with a thin rod, topped off by a force sensor. This force sensors is used to measure the excitation forces and is connected to the same DAQ as the accelerometers. The force sensor itself is attached to the specimen with a piece of double sided tape between them, to maintain continuous contact between the shaker and the specimen.

2.3. Results: modal shaker testing

In this section we will go over the resulting FRF of the shaker testing and determine the different elastic moduli. In total 9 different specimens were tested for each of the different printing directions. The FRF and Phase diagram for one of the nodes of a longitudinal specimen, are shown below in figures 2.9 and 2.10. These figures show the amplitude of the response for the selected output channels on a log-linear diagram as well as the phase of that response.

Figure 2.9: Frequency response function longitudinal direction

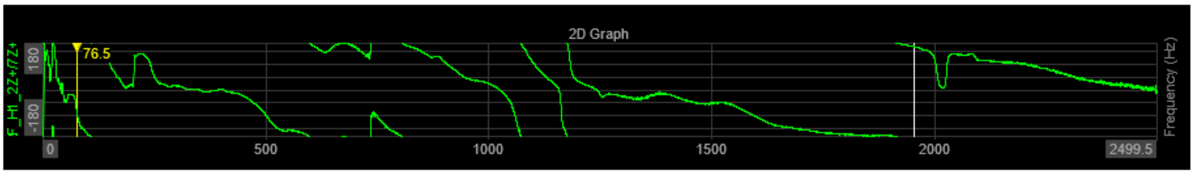

Figure 2.10: Phase diagram response function

The FRF (Frequency Response Function) displays the various resonance and anti-resonance peaks of the node in response to random excitation. The eigenfrequencies can be identified based on both a visible peak in the response function, as highlighted by the yellow line in Fig. 2.9, and the presence of a backwards phase shift in Fig. 2.10. During the measurements, a total of 10 or 11 FRFs were generated per specimen, each corresponding to the response of a single accelerometer. While it is possible to analyze each FRF separately, it was considered time-consuming and unneeded. The FRF's where combined into the CMIF(complex modal indicator function) shown in figure 2.11, where the peaks indicate the presence of a modal eigenfrequencies.

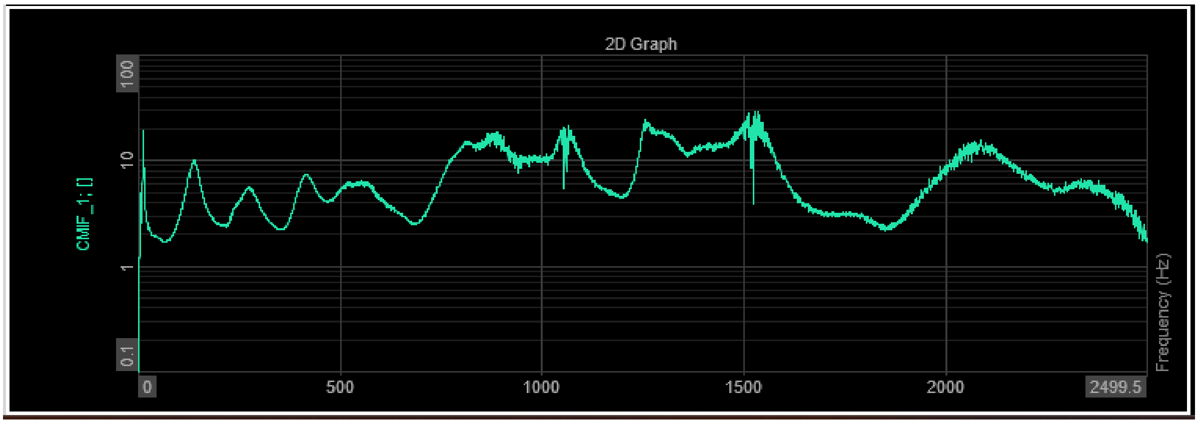

Figure 2.11: CMIF diagram

The peaks found in CMIF could be collected using the estimation function setting from Dewesoft. For the lower modes it was possible to directly identify them, but higher modes could only be identified as either being even or odd modes. This was done by looking at the phase difference between outer points. Using this method the following eigenfrequencies were found for each of the test setups.

Table 2.5: Bending eigenfrequencies in [Hz] found by the weighted shaker testing

Type	2b	3b	4b	5b	6b
L	10.35± 0.77	127.40± 8.57	247.27± 21.42	392.23± 31.42	532.13± 15.67
T	10.40± 0.94	126.28± 10.21	250.33± 8.39	366.70± 23.56	501.55± 13.78
O	10.39± 0.39	121.09± 6.10	235.23± 14.81	351.62± 22.76	499.32± 31.21

Type	7b	8b	9b	10b
L	654.24± 35.41	826.53± 42.25	914.60± 52.08	1249.22± 32.34
T	612.63± 25.42	851.38± 27.85	941.96± 67.81	1206.10± 16.08
O	606.22± 7.72	814.78± 39.78	886.63± 2.16	1127.50± 19.43

The same table values were also collected for the shear test setup.

Table 2.6: Bending eigenfrequencies in [Hz] found by the torsion type experiment

Type	2b	3b	4b	5b	6b
L	31.63 ± 2.60	82.83 ± 3.43	166.11 ± 8.60	271.06 ± 37.38	393.58 ± 15.51
T	33.79 ± 2.02	84.26 ± 3.37	158.14 ± 5.05	255.36 ± 38.45	389.13 ± 11.35
V	28.38 ± 4.18	82.63 ± 4.10	155.16 ± 17.85	250.98 ± 25.37	368.26 ± 10.42

Type	6b	7b	8b	9b
L	606.13 ± 31.11	741.81 ± 23.41	1023.40 ± 13.03	1249.80 ± 102.30
T	563.46 ± 51.74	719.63 ± 6.46	1024.74 ± 4.49	1233.00 ± 38.28
V	554.33 ± 32.01	724.39 ± 63.00	961.06 ± 70.11	1156.42 ± 67.65

In addition to the bending mode this test setup was also used to determine the torsional modes.

Table 2.7: Torsional eigen frequencies in [Hz] found by the shaker testing

Type	1t	2t	3t	4t	5t	6t	7t
L	46.83 ± 11.4	110.63 ± 9.0	218.25 ± 9.7	338.71 ± 19.1	621.42 ± 27.9	864.10 ± 20.9	1073.58 ± 13.3
T	41.95 ± 8.9	111.10 ± 27.3	207.05 ± 14.6	368.39 ± 2.7	607.50 ± 9.5	869.10 ± 15.0	1063.94 ± 15.8
V	44.17 ± 1.0	107.83 ± 22.2	204.52 ± 11.3	437.27 ± 28.8	639.69 ± 12.6	831.52 ± 26.8	1065.40 ± 18.7

As stated during 2.2 experimental theory, the thinned-walled nature of the specimens makes the assumptions of Euler beam theory untrue, so instead the program ANSYS MECHANICAL APDL was used to determine the resulting elastic moduli from the different eigenfrequencies using shell elements.

A total of six different Fem models were created, each with the different dimensions measured from the specimens as found in table 2.4. While it was initially proposed to use beam elements, the addition of bulkheads in between the specimens necessitated the use of shell elements, to properly model the behavior. In this regard, the element type SHELL181 was chosen for its use in structural analyses. Additionally the element type MASS21 was also used to add the masses of the accelerometers ad weights to the FEM. According to the manufacturer, these 352C22 type accelerometers weigh 0.5 grams [30], and with the total specimen weight of only 16 grams it was felt that their inclusion was necessary. For the geometry of the model the connecting sections of the specimen where modelled as twice the thickness of a regular wall section. This means that any effect of the added weight due to the superglue or improper bonding were ignored.

With the geometry sorted the next step is to mesh and run the model. For this the mesh size was set to 0.5 mm as was determine by a convergence study as partly seen in table 2.8 with a convergence criteria of 1% across all interested modes. With the next mesh size only differing by 0.58% the mesh size. The initial difference isn't only caused by a rough mess, the placement of the weight upon that rough mesh will also effect the outcome with finer meshes allowing more precise placement of the weights.

It should be noted that not all measured results will be used to determine the material properties. As higher modes are more difficult, both in their prediction using FEM's and their measurement in the dewesoft, the following modes where chosen for the measurements.

Table 2.8: Mesh convergency study interested modes of shear type experiment

Mesh size	2b	3b	4b	5b
0.0100	24.9726	68.8836	144.45	251.644
0.0050	25.56	70.54	147.84	250.62
0.0025	26.05	71.86	150.60	255.17
0.0013	26.23	72.33	151.48	256.73
0.0006	26.30	72.57	151.90	257.23

Mesh size	1t	2t	3t	4t
0.0100	38.32	84.45	176.97	320.982
0.0050	42.15	94.53	196.83	337.07
0.0025	40.81	91.18	190.06	335.93
0.0013	41.22	92.60	193.31	336.50
0.0006	40.98	92.26	192.95	336.28

The MAPDL code itself was run via a script in python that would automatically generate different values of the Young's modulus and Shear modulus and then put them in different text files to be run. These files were then run individually within Mechanical APDL and the output was saved. The Python code and an example MAPDL code can be seen in appendix B. To determine the uncertainty of the found Young's moduli it was decided to use first order error propagation which was done with the derivative of the frequency-stiffness dependency curve found.

One of the generated geometries can be seen in figure 2.12.

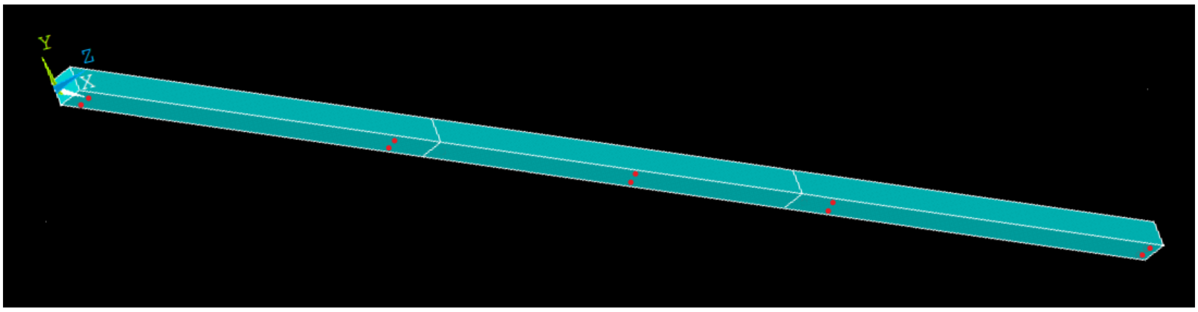

Figure 2.12: Pre-mesh MAPDL geomertry

Using the first natural frequency to determine the material properties for the two different testing methods, the results from APDL are as follows.

Table 2.9: Comparison between predicted eigenfrequencies of ANSYS and the measured eigenfrequencies (exp) in Hz with constant young modulus

	Longitudinal	E=1.74e9	G = 6.92e8	Transversal	E=1.82e9	G = 3.47e8	Vertical	E = 1.29e9	G = 3.6e8
Mode type	Ansys Hz	Experimental [Hz]	Error %	Ansys Hz	Experimental [Hz]	Error %	Ansys Hz	Experimental [Hz]	Error %
2b	31.64	31.63	0.0%	33.79	33.79	0.0%	28.33	28.38	-0.2%
3b	87.34	82.83	5.5%	92.37	84.26	9.6%	77.49	82.63	-6.2%
4b	182.83	166.11	10.1%	190.34	158.14	20.4%	159.76	155.16	3.0%
5b	308.17	271.06	13.7%	317.44	255.36	24.3%	267.27	250.98	6.5%
t1	46.77	46.83	-0.1%	41.94	41.95	0.0%	44.20	44.17	0.1%
t2	107.42	110.63	-2.9%	101.71	107.58	-5.5%	99.24	107.83	-8.0%
t3	227.90	218.25	4.4%	221.42	203.98	8.6%	204.15	203.17	0.5%
t4	400.77	338.71	18.3%	392.73	376.45	4.3%	346.07	437.27	-20.9%

Table 2.10: Comparison between predicted eigenfrequencies of ANSYS and the measured eigenfrequencies (exp) in Hz for the weighted testing

	Longitudinal	E = 1.54e9	G 4.1e8	Transversal	E=1.365e9	3.60E+08	Vertical	E = 1.31e9	G = 3.3e8
Mode type	Ansys Hz	Experimental [Hz]	Error %	Ansys Hz	Experimental [Hz]	Error %	Ansys Hz	Experimental [Hz]	Error %
2b	10.38	10.35	0.2%	10.42	10.40	0.2%	10.35	10.39	-0.4%
3b	63.06	127.40	-50.5%	61.26	126.28	-51.5%	59.52	121.09	-50.8%
4b	103.21	247.27	-58.3%	100.77	250.33	-59.7%	97.73	235.23	-58.5%
5b	239.39	392.23	-39.0%	235.41	366.70	-35.8%	224.49	351.62	-36.2%
6b	303.91	532.13	-42.9%	297.12	501.55	-40.8%	289.95	499.32	-41.9%
7b	375.76	654.24	-42.6%	355.82	612.63	-41.9%	356.63	606.22	-41.2%

From these results it should be clear that there is something wrong with the eigenfrequencies of the weighted measurements. When one looks at the eigenfrequencies of a system with added masses one would expect lower eigenfrequencies for the same modes. However looking at the frequencies in the tables above, this is only the case for the first mode. The other modes are higher then their equivalent in the 'shear' tests. Theses deviations are also found when looking at the results from ANSYS where second mode is at 63 Hz instead of the 127 Hz measured. Because of these facts it is concluded that there was a error in the measurements of the weighted modes. The near identical setups between the different modes makes it difficult to say were the error could arise from. It is assumed at this point that the error is due to a way the masses were added to the specimens.

Frequency dependency.

The above values where for a constant Young's Modulus across the frequency range. But we also wished to investigate the frequency dependency of the material. In order to do this the Young's modulus of the Fem was changed so that the predicted mode matched that of the measured results. This was then noted down and the Young's modulus was plotted against the frequency. But before we can say anything about the frequency dependency of the response we need to determine a elastic model with which to curve fit these points. For Thermoplastics there are several options [31]. It was decided to use The basic the kelvin model also know as the Voigt-kelvin model. This model consist of a linear elastic part and a dashpot/viscous part placed in parallel. Other models such as the Maxwell and the

Weichert model were also considered but were either focused upon creep or meant for thermoset plastics respectively.

The relationship between the complex dynamic modulus and the frequency for this type of material is as follows:

$$E^*(\omega) = E_0(1 + i\omega\tau) \tag{2.32}$$

Were ω is the excitation frequency and $\omega\tau$ is the loss modulus, this means that there is a linear relationship between the Young's modulus and frequency. Using this relationship the following trend lines were plotted.

The determined material values can be found in table C.1 in appendix C.

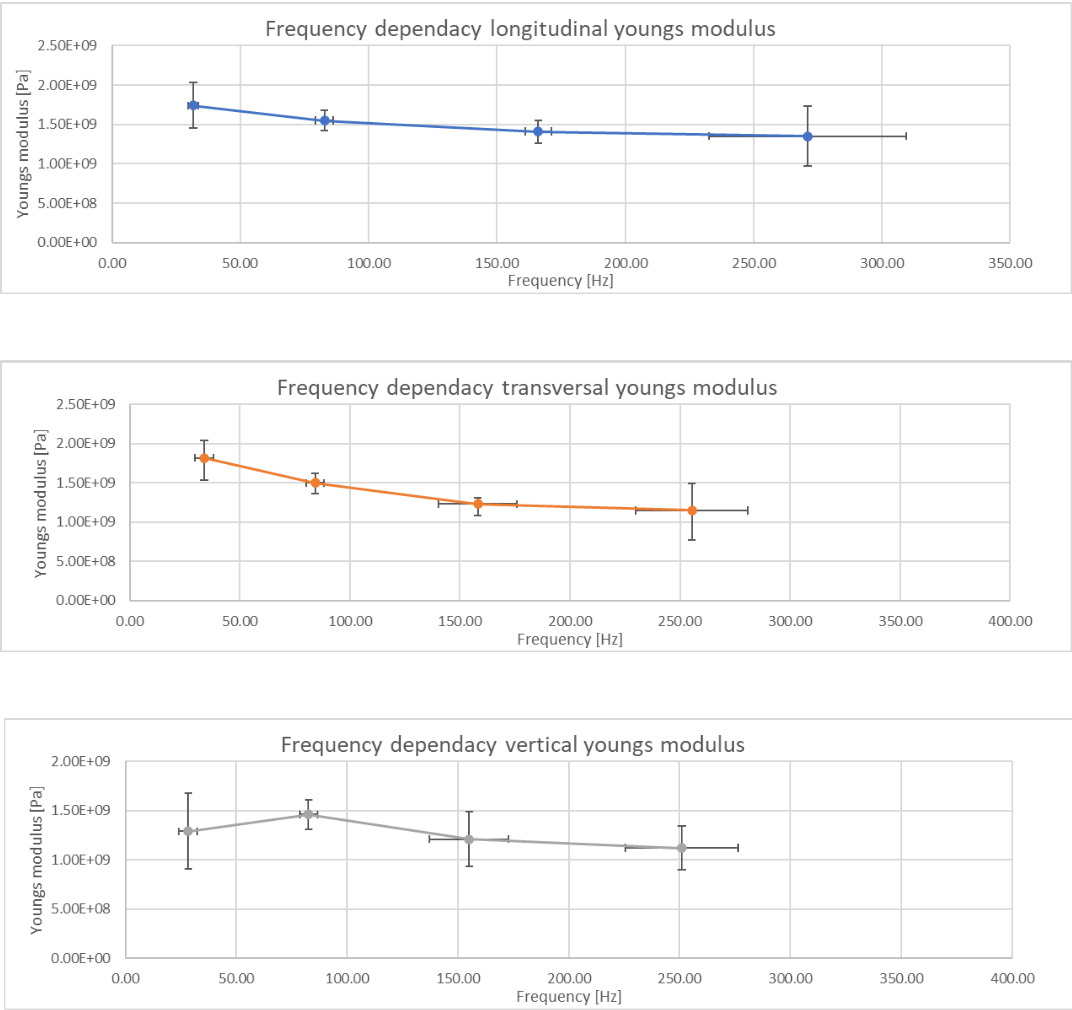

Figure 2.13: Measured frequencies dependant flexural modulus

Plotting all results in the same graph without the deviation range, results the following graph with trend lines.

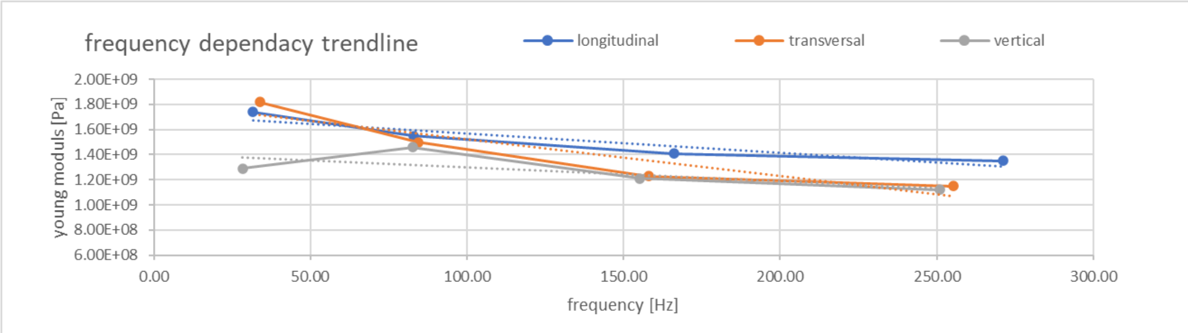

Figure 2.14: Flexural modulus

In addition to the Young's modulus we will also plot the shear modulus using the Voigt model which is practically the same except for the use of torsional elements.

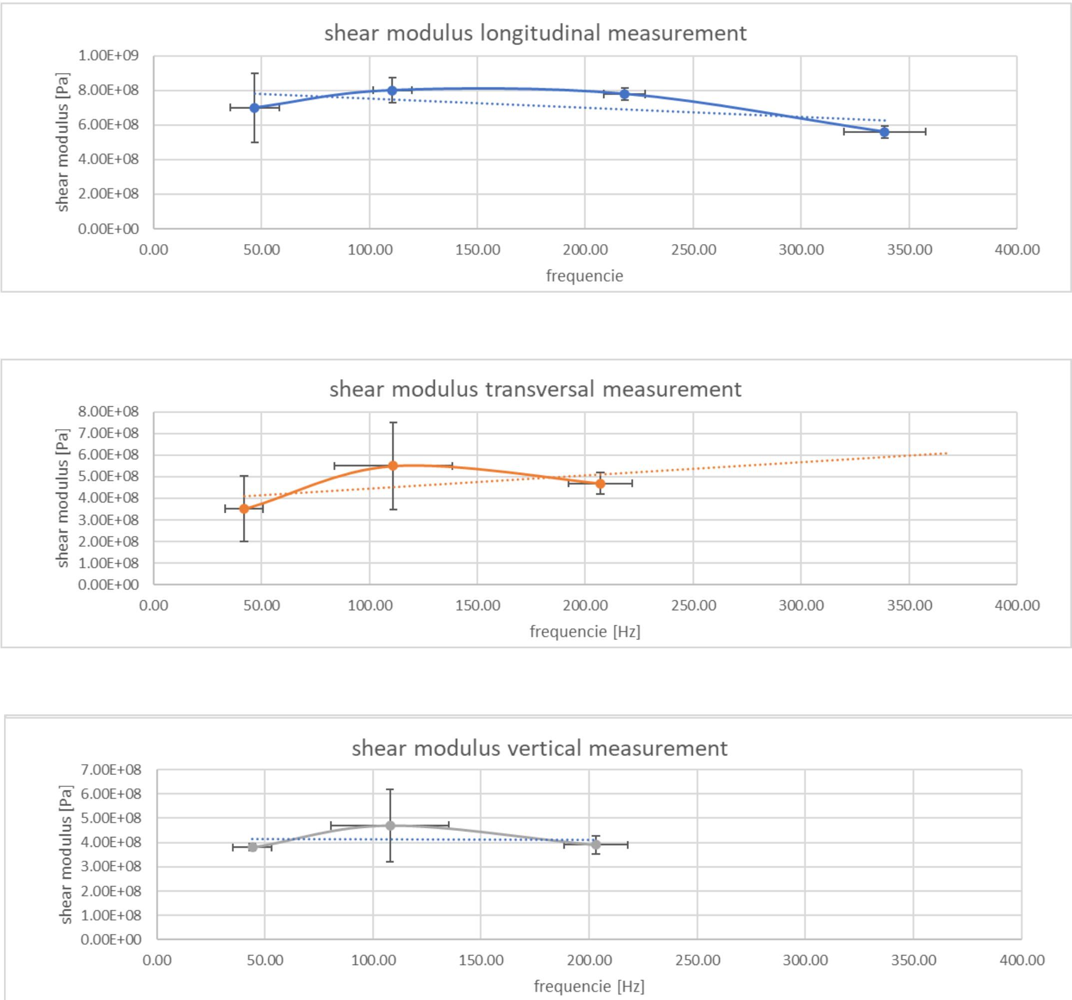

Figure 2.15: Measured frequencies dependancy shear modulus

The shear moduli plotted in the figures above where obtained with the Young's moduli at the eigenfrequencies but their values are impossible. The range of values is to large and some values would cause negative Poisson ratio's to the points that the fourth torsional mode require a higher shear moduli then Young's moduli. Because of this it was decided to use a set Poisson ratio of 0.33 and calculate the shear moduli from the Young's moduli with that Poisson ratio, instead of working with the measured results.

The final material properties are as follows:

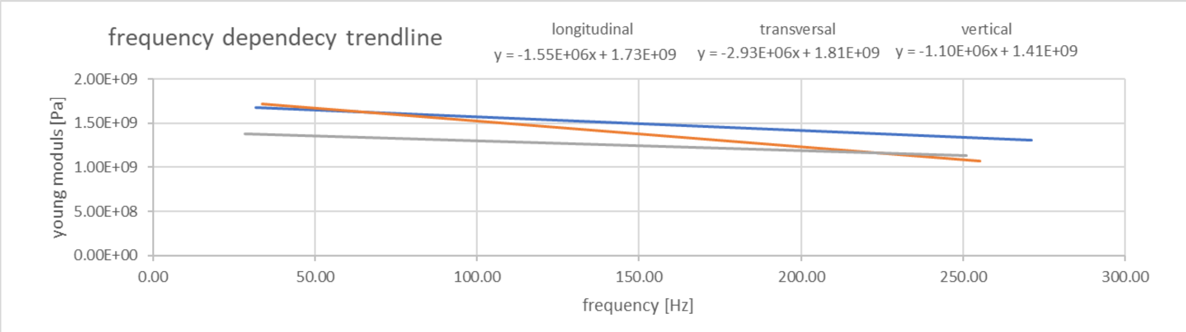

Figure 2.16: Chosen trend lines for flexural moduli

Using the Poisson ratio the shear moduli are as follows.

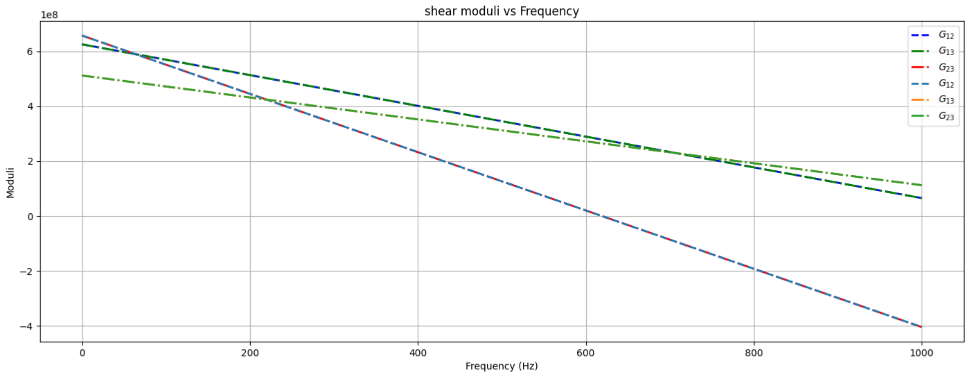

Figure 2.17: Chosen trend lines for shear moduli

Using the frequency dependency the first four frequencies are found and compared to the measured results.

Table 2.11: Torsional eigen frequencies in [Hz] found with frequency dependent Young's moduli

	Longitudinal	E=1.74e9	G = 6.92e8	Transversal	E=1.82e9	G = 3.47e8	Vertical	E = 1.29e9	G = 3.6e8
Mode type	Ansys Hz	Exp [Hz]	error %	Ansys Hz	Exp [Hz]	error %	Ansys Hz	Exp [Hz]	Error %
2b	31.07	31.63	-1.8%	32.41	33.79	-4.1%	29.33	28.38	3.3%
3b	83.65	82.83	1.0%	85.64	84.26	1.6%	78.68	82.63	-4.8%
4b	167.74	166.11	1.0%	163.78	158.14	3.6%	157.03	155.16	1.2%
5b	267.51	271.06	-1.3%	249.30	255.36	-2.4%	251.93	250.98	0.4%
t1	43.89	46.83	-6.3%	52.63	41.95	25.5%	50.74	44.17	14.9%
t2	99.44	110.63	-10.1%	110.80	107.58	3.0%	108.12	107.83	0.3%
t3	202.22	218.25	-7.3%	204.95	203.98	0.5%	207.44	203.17	2.1%
t4	332.05	338.71	-2.0%	302.33	376.45	-19.7%	324.36	437.27	-25.8%

2.4. Reflection upon experiments.

During the process of determining the material properties, various experimental setups were used. Some produced useful results, while others did not, highlighting areas where improvements or changes could be made. This section will discuss the different experiments, detailing what worked and what didn't.

As stated earlier, the initial modal analysis was attempted with an impact hammer instead of a modal shaker. However, several factors prevented this method from producing usable results. The first issue was the boundary conditions of the specimen. Initially, it was thought that the specimen could be clamped to a surface, to mimic a clamped-free condition. However, the necessary clamping force to achieve a clamped condition would cause the thin walls of the specimen to buckle and crush. This might bee mitigated by partially filling the specimen with a 100% infill for 1 cm, which could withstand the clamping force without being crushed. However, this approach introduced a discontinuity in the structure.

Instead, a different boundary condition was attempted: a free-free condition. First, the specimen was placed on a foam pad and tested with the impact hammer. Here, it was found that the specimen would jump unpredictably and was more fragile than initially anticipated. In one of the exploratory trials, an impact split the specimen's walls, resulting in the loss of that particular sample. Additionally, an attempt was made to suspend the specimen in the air with elastic bands. This method also failed, as it was difficult to strike the specimen with sufficient force, and repeated hits did not produce any clear mode shapes in Dewesoft. It is suspected that this was due to the difficulty in striking the same spot consistently on a swaying, lightweight beam.

This led to the selection of the shaker method to excite the different specimens. Here, also, different setups were used as discussed above. For the weighted approach, it became clear that adding weights altered the boundary conditions, making it no longer a true free-free condition. It is suspected that the weight ratio between the specimen and the added masses caused the weights to act as boundary constraints. With the weights being 6 times the weight of the beam. Since the purpose of adding weights was to further reduce the eigenfrequency to below 10 Hz, future attempts to achieve such a low eigenfrequency should instead increase the specimen length rather than adding weights. The modal shaker was also used for the torsion experiment, which aimed to measure the shear moduli of the specimen. However, it was only successful in determining the Young's modulus. This may be due to a combination of the attachment method used for the shaker and the principles of Saint-Venant's theory. For the torsion setup, double-sided tape was used to attach the force sensor of the shaker to the top of one of the side walls. Although it was checked that the attachment was secure both before and after each measurement, the contact surface was quite small. Since the force sensor allows for different attachment heads, it might be possible to machine a better attachment for the shaker in future experiments. Additionally, an alternative method for determining Gxy, Gxz and Gyz from the measured stiffness is needed. With the current approach, which relies on the assumptions of both orthotropic and isotropic behaviour, the calculated Poisson's ratios are below 0 which is outside the expected range of 0.2-0.4.

While there were reasons for the way the specimen was designed, in any future study one would seriously have to consider a different design. Due to the thin nature of the specimens small imperfections often caused the loss of the whole specimen. As a small break of blob would lead to disintegration the rest of the wall at that point. In addition it might also be wise to consider the nozzle size when deciding the scale of the model. The reason for this is that during the print, the 0.25 mm nozzle was prone to clogging, which can cause problems if one were to attempt to print larger sections. When designing their specimen one should also take into account what they are measuring. As the current one size fit all approach doesn't leads to optimal results for any of searched after variables.

The measured value of the flexural moduli we found (1.41-1.81 MPa) is above the expected range that the producer of the PETG filament stated in its technical documentation (1.07 MPa) [32]. While some change compared tot the base material could be expected due to uncertainty in the testing method. The degree seen here indicates some process is hardening the material to a significant degree.

For future work it might be worth looking into a different testing method all together. Even if the current method is successfully, there is only a limited amount of points in the frequency range for which the moduli can be determined. A method using bulk wave experiments or guided wave experiment would allow for the determination of the Young's modulus for a continuos frequency sweep instead of the different setups which are needed for the current setups to get multiple points in the wanted frequencies band. However the reasons for not choosing those method would still need to be addressed. While bulk wave type experiments allow for the measurement of the speeds of P and S type waves though a material, which allows for the measurement of both bulk and shear moduli, those waves require thick section to move through for proper measurement which would required the dropping of the thin walled nature of the material research additionally the internal structure of 3D printed material could cause the waves to internally reflect. It does appear however that it is possible to test in the interested frequency range as [11] shows that it's possible to use DMA and measure the complex youngs modulus between 0.1 and 100 Hz.

2.5. Conclusion

The purpose of this chapter was to explain why and how the material properties of PETG were obtained using modal analysis for a model scaled with Froude scaling.

The chapter begins by outlining the method used to scale down the structural stiffness for a fully flexible model using Froude scaling. It explains how the total stiffness of a scaled-down section depends on the Young's modulus of the material for the scaled model. Next, the experimental theory covers the relationship between the eigenfrequency and the Young's/shear modulus, including the use of Saint-Venant theory to determine the shear moduli G12 ,G13 and G23 from the measured GL GT, and GV. This approach to determine the shear modulus did not produce usable results.

The chapter then details the various experimental setups used during the modal analysis. Beginning with the design of the specimen, initial attempts were made using an impact hammer, but ultimately a shaker was chosen for its more consistent results. It was found that the weighted approach somehow increased the eigenfrequencies of the 2nd and 3rd modes compared to the unweighted approach, likely due to the large mass ratio of the weights relative to the hollow beams. Consequently, only the unweighted frequencies were used to determine the Young's moduli.

These frequencies were converted into Young's moduli using a FEM, from which it was found that the vertical Young's modulus was 75% of the longitudinal and transversal moduli. For frequency dependency, it was observed that at higher frequencies, there was a decrease in the measured moduli.

For future research into the frequency dependency of 3D-printed materials, it is recommended to use either bulk or guided wave experiments, as these methods allow for a continuous frequency domain to be investigated, rather than being limited to the three points which was aimed for with the current method. Bulk waves measurements may also enable direct measurement of the shear moduli, avoiding the need for calculations based on Saint-Venant theory.

3

FEM model

Investigating the effect of the orthotropic and frequency-dependant material value with the physical model shown in figure 2.1 would be difficult as there is no orthotropic model to compare to. Helpfully A. Keser also created a complete Finite Element Model (FEM) of the catamaran 3.1. This chapter will go into detail how the material values determined in the last chapter were applied to the FEM. And how the effect of the surrounding water was accounted for in the resulting analysis of the model.

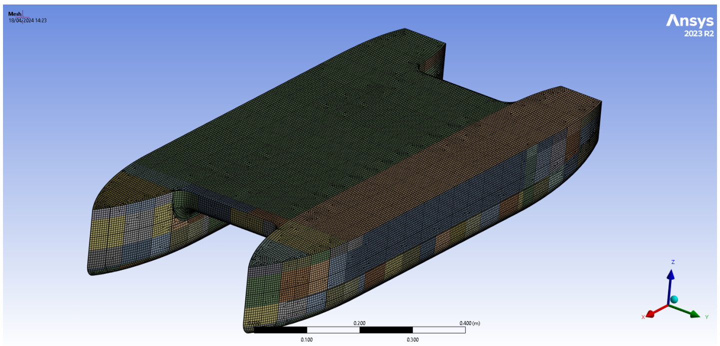

Figure 3.1: MESH scaled model

3.1. Model for orthotropic behaviour

As stated in the design guide lines for the vibration specimens 3D printed structures consist of 2 different structural types that effect the elastic properties: the outer lines, a.k.a. the perimeter, highlighted with red in figure 3.2 and the internal structure, a.k.a. the infill, highlighted in figure 3.8. While both of these structures are anisotropic, they do differ with the perimeters acting like fully orthotropic and the infill acting more like a transverse isotropic material.

3.1.1. Orthotropic model - walls

Figure 3.2: Perimeters of 3D print

Using the material values gathered in 2.2, we can construct a stiffness matrix. This shows the elastic relationship between stress and strain for each of the principal directions of the 3D printed structure. This matrix [C] is referred to as the compliance matrix.

$$\begin{bmatrix} \epsilon_1 \\ \epsilon_2 \\ \epsilon_3 \\ \gamma_{23} \\ \gamma_{13} \\ \gamma_{12} \end{bmatrix} = \begin{bmatrix} \frac{1}{E_1} & -\frac{\nu_{21}}{E_2} & -\frac{\nu_{31}}{E_3} & 0 & 0 & 0 \\ & \frac{1}{E_2} & -\frac{\nu_{32}}{E_3} & 0 & 0 & 0 \\ & & \frac{1}{E_3} & 0 & 0 & 0 \\ & & & \frac{1}{G_{23}} & 0 & 0 \\ & sym & & & \frac{1}{G_{13}} & 0 \\ & & & & & \frac{1}{G_{12}} \end{bmatrix} \begin{bmatrix} \sigma_1 \\ \sigma_2 \\ \sigma_3 \\ \tau_{23} \\ \tau_{13} \\ \tau_{12} \end{bmatrix} \tag{3.1}$$

Using this matrix, we predict the elastic deformation of a orthotropic material. However this compliance matrix can only be used for the main coordinate system of the material. This is only the case in straight walls without any overhang, requiring us to transform the compliance matrix to fit the different local coordinate systems that are present in our model. Simple 90° rotation can be used for straight walls and single layer thick floors. The stiffness matrix must be transformed for the other curved walls. To transform the stiffness matrix accordingly, we will be using a transformation matrix as explained by [22]. This method works by transforming the stress and engineering strain using a transformation matrix[T]. This matrix is determined by the angle from each coordinate axis from the material(123), to the axes of the local coordinate system(xyz). This results in a total of nine angles to consider. Three of the angles are shown in figure 3.3. A quick way of determining these angles is the use a rotation matrix for a 3 dimensional system. After this we use the dot product to find the angles needed in table 3.3.

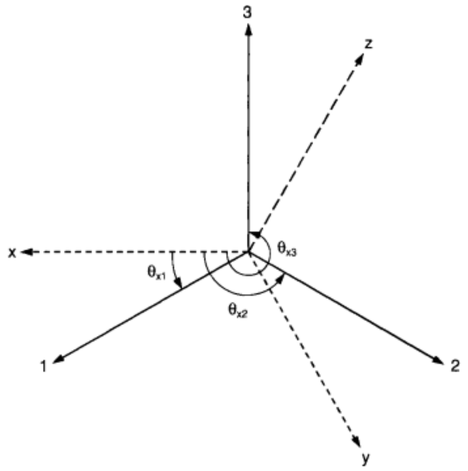

Figure 3.3: Rotation angles form x-axis [22]

$$\begin{aligned} m_1 &= cos(\theta_{x1}) & n_1 &= cos(\theta_{y1}) & p_1 &= cos(\theta_{z1}) \\ m_2 &= cos(\theta_{x2}) & n_2 &= cos(\theta_{y2}) & p_2 &= cos(\theta_{z2}) \\ m_3 &= cos(\theta_{x3}) & n_3 &= cos(\theta_{y3}) & p_3 &= cos(\theta_{z3}) \end{aligned} \tag{3.2}$$

$$[T] = \begin{bmatrix} m_1^2 & n_1^2 & p_1^2 & 2n_1p_1 & 2p_1m_1 & 2M_1n_1 \\ m_2^2 & n_2^2 & p_2^2 & 2n_2p_2 & 2p_2m_2 & 2M_2n_2 \\ m_3^2 & n_3^2 & p_3^2 & 2n_3p_3 & 2p_3m_3 & 2M_3n_3 \\ m_2m_3 & n_2n_3 & p_2p_3 & n_2p_3 + n_3p_2 & p_2m_3 + p_3m_2 & m_2n_3 + m_3n_2 \\ m_3m_1 & n_3n_1 & p_3p_1 & n_3p_1 + n_1p_3 & p_3m_1 + p_1m_3 & m_3n_1 + m_1n_3 \\ m_1m_2 & n_1n_2 & p_1p_2 & n_1p_2 + n_2p_1 & p_1m_2 + p_2m_1 & m_1n_2 + m_2n_1 \end{bmatrix} \tag{3.3}$$

This transformation matrix works with engineering strains which differ from the tensoral strain vector in 3.1 by a factor of 2 for the shear strain, requiring us to transform the tensoral strain into the engineering strain with matrix [L].

$$[\epsilon]_{engineering} = [L][\epsilon]_{tensoral}$$
$$\begin{bmatrix} \epsilon_x \\ \epsilon_y \\ \epsilon_z \\ \gamma_{yz} \\ \gamma_{xz} \\ \gamma_{xy} \end{bmatrix} = \begin{bmatrix} 1 & & & & & \\ & 1 & & & & \\ & & 1 & & & \\ & & & 2 & & \\ & & & & 2 & \\ & & & & & 2 \end{bmatrix} \begin{bmatrix} \epsilon_x \\ \epsilon_y \\ \epsilon_z \\ 0.5\gamma_{yz} \\ 0.5\gamma_{xz} \\ 0.5\gamma_{xy} \end{bmatrix} \tag{3.4}$$

In order to transform the strain from 3.1, we first change it into a tensoral strain, followed by a transformation with [T], and then turn it back to an engineering strain which looks as follows:

$$[\epsilon_{123}] = [L][T][L]^{-1}[\epsilon_{xyz}] \tag{3.5}$$

The transformation of the stress is easier and looks as follows

$$[\sigma_{123}] = [T][\sigma_{xyz}] \tag{3.6}$$

Combining 3.1, 3.5 and 3.6 we acquire the following results for the compliance matrix in any direction.

$$\begin{aligned} [\epsilon_{123}] &= [C][\sigma_{123}] \\ [L][T][L]^{-1}[\epsilon_{xyz}] &= [C][T][\sigma_{xyz}] \\ [\epsilon_{xyz}] &= ([L][T][L]^{-1})^{-1}[C][T][\sigma_{xyz}] \\ [C_{xyz}] &= [L][T]^{-1}[L]^{-1}[C][T] \end{aligned} \tag{3.7}$$

With this methode we can rewrite equation 3.1 to the following arbitrary coordinate system XYZ

$$\begin{bmatrix} \epsilon_x \\ \epsilon_y \\ \epsilon_z \\ \gamma_{yz} \\ \gamma_{xz} \\ \gamma_{xy} \end{bmatrix} = \begin{bmatrix} C_{11} & C_{12} & C_{13} & C_{14} & C_{15} & C_{16} \\ C_{21} & C_{22} & C_{23} & C_{24} & C_{25} & C_{26} \\ C_{31} & C_{32} & C_{33} & C_{34} & C_{35} & C_{36} \\ C_{41} & C_{42} & C_{43} & C_{44} & C_{45} & C_{46} \\ C_{51} & C_{52} & C_{53} & C_{54} & C_{55} & C_{56} \\ C_{61} & C_{62} & C_{63} & C_{64} & C_{65} & C_{66} \end{bmatrix} \begin{bmatrix} \sigma_x \\ \sigma_y \\ \sigma_z \\ \tau_{yz} \\ \tau_{xz} \\ \tau_{xy} \end{bmatrix} \tag{3.8}$$

With this compliance matrix we can now model the elastic moduli in any of the local coordinate systems. As stated before this can be used to model the walls of the printed structure by rotating around the vertical axis. A rotation around the transversal axis is used to account for the curving of the hull and the middle deck. Figure 3.4 shows how the elastic moduli differ with rotation around the longitudinal axis, with 3.5 and 3.6 showing the rotation over the transversal and vertical axis, based upon the material values at 40 Hz.

Table 3.1: Material values at 40 Hz

Elastic moduli	E_1	E_2	E_3	nu_12	nu_13	nu_23	G_12	G_13	G_23
1b	1.66e9	1.70e9	1.37e9	0.38	0.38	0.38	6.03e8	6.03e8	6.15e8

These material values were used with the internal structure of the model (see 3.10) and the skin of the model without an epoxy layer.

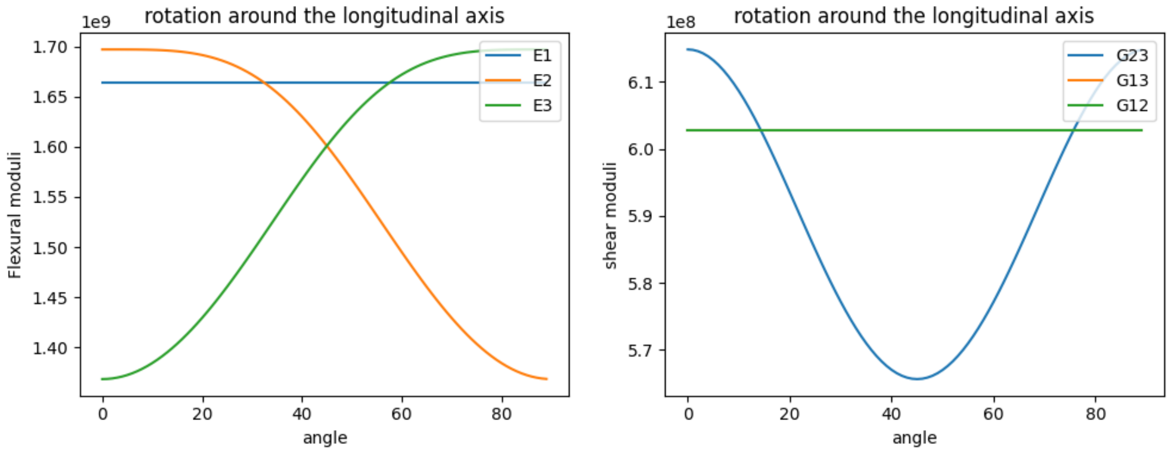

Figure 3.4: Plots of of the elastic moduli as rotated around the longitudinal axis at 40 Hz

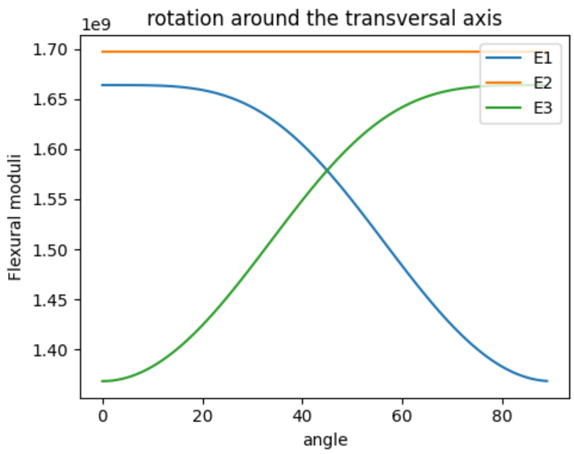

(a) a

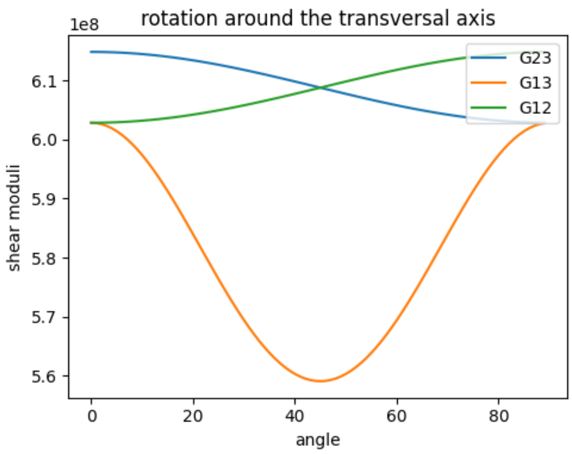

(b) b

Figure 3.5: Plots of of the elastic moduli as rotated around the transversal axis at 40 Hz

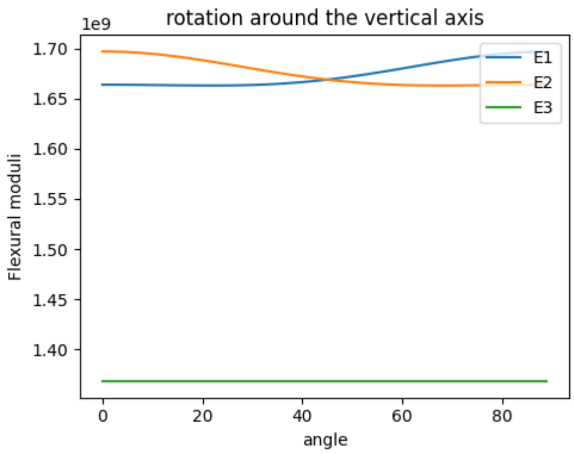

(a) a

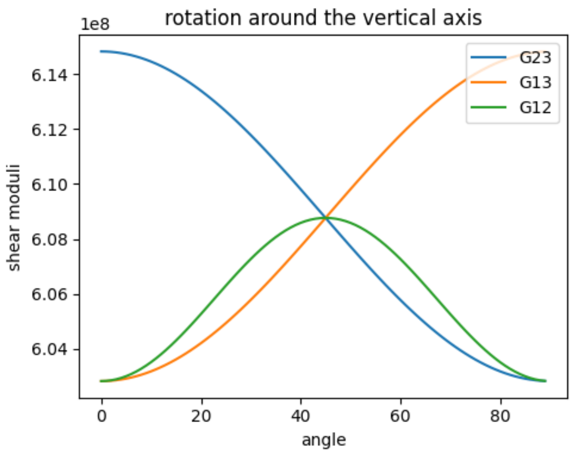

(b) b

Figure 3.6: Plots of of the elastic moduli as rotated around the vertical axis at 40 Hz

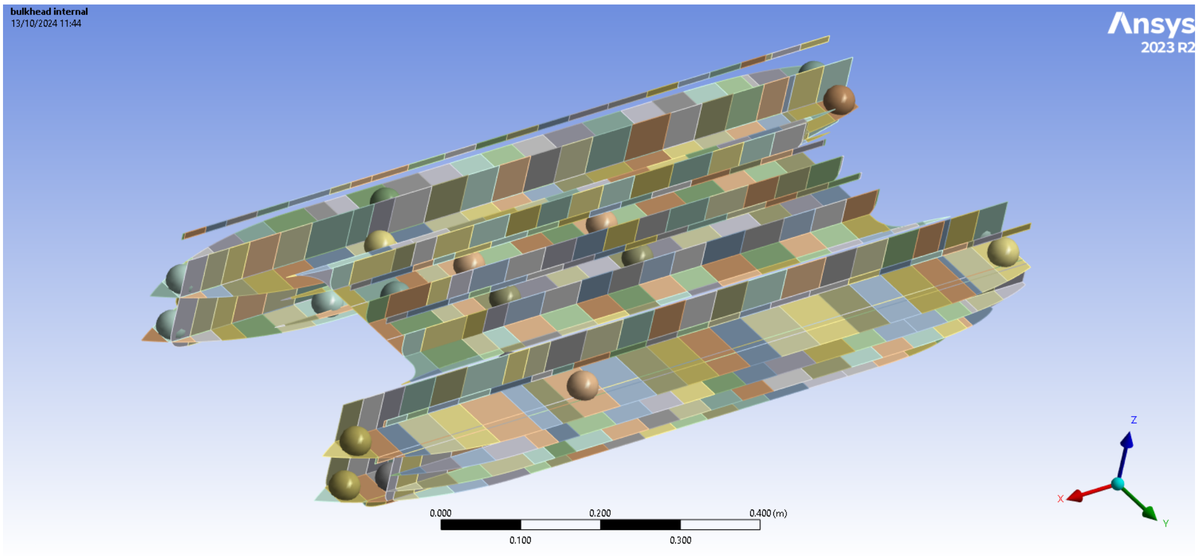

Figure 3.7: Internal walls modeled as orthotropic material

3.1.2. Composite - bulkheads and web frames

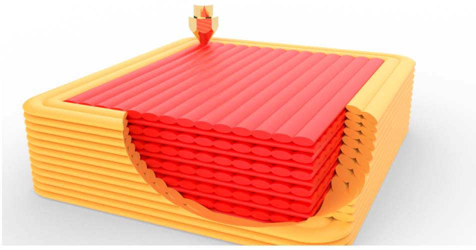

Figure 3.8: Infill 3D print

The second type of material is the infill. This is used to fill most of the internal volume of any print. Normally this consists of around 3–7 solid layers, followed by layers that are hollow, and finally again 3–7 layers of solid infill to cap off. Due to the thin walled nature of the model created by A. Keser, this middle layer is absent. Instead the bulkhead and other horizontally printed elements were solid.

In order to model the elastic characteristics we could use the composite theory from [22]. However this theory is based upon a 2D plane and assumes that the mid-plane is inextensible e.i. $\epsilon_{zz} = 0$ and does not account for the torsion or bending in the third plane.

Instead the ACP-pre module of Ansys Mechanical will be used to determine the material values in all directions. This allows for a direct definition and use of the laminate material within the same program. However to do so we first need to determine the first layup of the infill. As this will determine the orientation of the individual layers. The default layup settings for most slicers use a repeating [45,-45] pattern for the layup relative to the build plate. The average thickness of a bulkhead was 0.56 mm [2] and with a layer thickens described before, a total of 4 layers should be present with the following layup and thicknesses: [-45,45,-45,45], [0.15,0.125,0.125,0.125]. The measured difference in total thickness could be caused by uncertainty in the thickness of the different layers as was found in [2].

These layups were recreated within the ACP module and the resulting material values extracted and applied to the horizontally printed bulkheads as an orthotropic material. It was initially attempted to apply the ACP module directly to the model of [2] but this caused the numerical model to no longer work. The cause of which was discovered to late in the process to address. This had two consequences: the vertical Young's modulus for stacking direction had to be determine by spring in series theory and the coupling between bending and tension present in composite structures is neglected. This results in the following elastic properties for the layup for the bulkheads at 40 Hz.

Table 3.2: Material values of the bulkheads at 40 Hz

Elastic moduli	E_1	E_2	E_3	nu_12	nu_13	nu_23	G_12	G_13	G_23
value [Pa]	1.67e9	1.67e9	1.37e9	0.39	0.37	0.37	6.07e8	6.09e8	6.09e8

These material values were used with the internal bulkheads of the model (see 3.10) and the rear of the model without an epoxy layer.

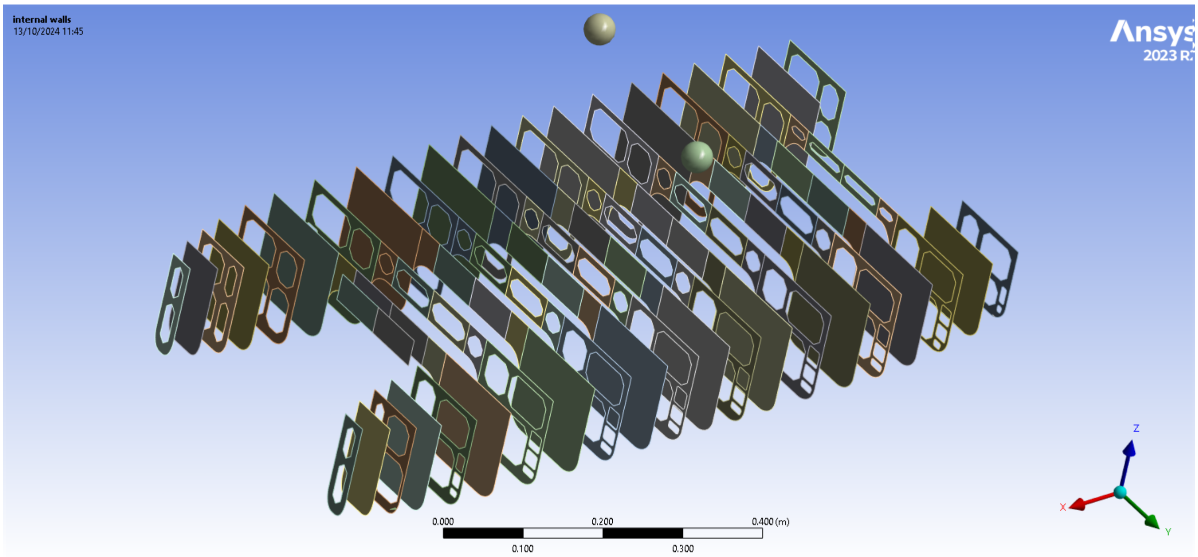

Figure 3.9: Internal bulkhead modeled as composite structures

3.1.3. Composite - epoxy coated structure

In addition to the bulkheads, the outer layer of the model also consisted of multiple layers. When constructing the initial model A. Keser joined the individual section with the use of epoxy resin. Additionally to waterproof the structure a final layer of epoxy was applied around the whole model. The total weight of resin added was 140g. Because this resin was added to the outside and could also effect the response, it will also be accounted for in the numerical model.

The resin used was poly service THV-500 and harder 355. We used the material properties found on polyservice.nl [33], which state that the hardened epoxy has a Young's modulus of 2.6e9 Pa and an assumed Poison ratio of 0.33. The surface area of the scale model is 1415181.61 mm^2 as measured from the Rhino model provided by A. Keser. This together with the density given by the manufacturer of 1.1 $[g/cm^3]$ give a average thickness of 0.089 mm. This means that the layup for the sections which have epoxy coating is as follows: [0.53,0.089] mm for the skin and the local rotation and [0.089,0.15,0.125,0.125,0.125,0.125] mm for the stern of the model.

This gives the following material values for the skin 3.3 and the stern 3.4 of the model:

Table 3.3: Material values of the epoxy coated bulkhead at 40 Hz

Elastic moduli	E_1	E_2	E_3	nu_12	nu_13	nu_23	G_12	G_13	G_23
	1.79e9	1.79e9	1.44e9	0.38	0.35	0.35	6.52e8	6.62e8	6.62e8

Table 3.4: Material values of the epoxy coated skin at 40 Hz

Elastic moduli	E_1	E_2	E_3	nu_12	nu_13	nu_23	G_12	G_13	G_23
	1.77e9	1.76e9	1.50e9	0.35	0.37	0.34	6.52e8	6.43e8	6.59e8

These material values were used with the skin of the model, where the epoxy is present.

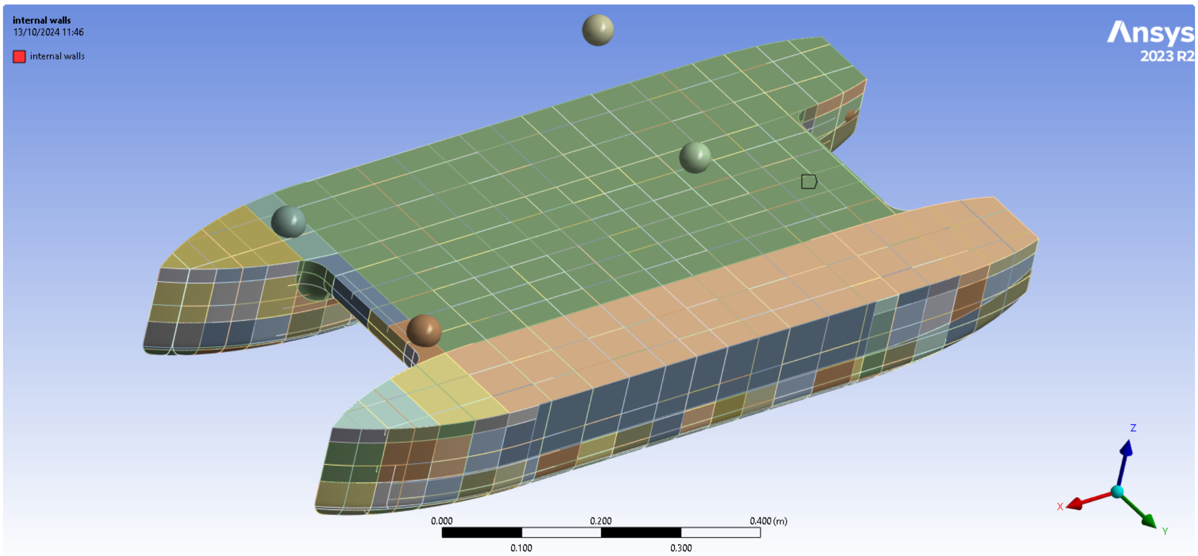

Figure 3.10: Skin section modelled with epoxy.

3.2. Added Mass of surrounding water

With the material properties of the elastic model now fully defined we can predict the "dry" response of the model. However as the elastic model is meant for use within a towing tank to predict the hydro dynamic interaction, we will also include effects of the surrounding water to mimic the "wet" response. The method by which the hydro elastic interaction is modelled with numerical analysis is based upon the framework presented by [34] and [35], the latter of which is a fellow master student who was able to provide in-depth explanation of the method and a code modified to the need of this project.

3.2.1. 3D structual model

The numerical analysis is based on mode superposition and consists of three components: a 3D structural model, a 3D hydrodynamic model and lastly a iterative procedure for a 'wet' eigenvalue analysis.

The 3D structural model in our case is A. Keser's model, modified with the material properties found above. This model was meshed with square shell elements. Initially it was thought that it might be possible to cut the model in two to save calculation power, but it was found that the eigenmodes which where of interest to us weren't symmetrical in the XZ-plane of the model. What was simplified were the structures of the crane and tower, located on the deck of the model. These were replaced with point masses that where constrained to the deck surface, as we are mostly interested in the dynamics of the hull.
In the structural model the only forces that are present are those of the structure itself. This means there is no influence of hydrodynamic dampening or hydro static stiffness making this the 'dry' eigenvalue analysis. With the only forces present in the model being the inertia of the model and the stiffness of the material, neglecting external forces and damping as we did with the material properties. Based on this Newtons second law looks like:

$$\mathbf{M}^{str}\mathbf{U}''_{dry} + 0 + \mathbf{K}^{str}\mathbf{U}_{dry} = 0 \tag{3.9}$$

With **U** being the degree of freedom for each element in the model and **M** and **K** being the structural mass and stiffness matrices. Similar to the way that the 2D beams modal shape consisted of a time dependant part and a location dependant part, we can assume the degree off freedom to consist of a time/frequency dependant part and the eigenvectors. By splitting these up and taking the derivative we can rewrite the above equation as follows.

$$(\mathbf{K}^{str} - (\omega^{str})^2\mathbf{M}^{str})\Phi = 0 \tag{3.10}$$

Where ω^{str} are the eigen frequencies and Φ is the eigenvector matrix from which we can get the dry eigen mode. By extracting the values for the degrees of freedom in x,y, and z for each point we can find Φ_x, Φ_y, Φ_z for the dry isotropic model which are the displacements in x,y and z for each point. The first 10 frequencies are shown below.

Mode	rigid-1	rigid-2	rigid-3	rigid-4	rigid-5	rigid-6	flex-1	flex-2	flex-3	flex-4
Freq[Hz]	0	0	0	0	0	0	25.507	28.095	46.358	50.657

Table 3.5: 'Dry' eigen frequencies of orthotropic model

Because of the lack of outside forces the model is free to move in any direction without a restoring force. This means that the translation and rotation in the 6 degrees of freedom are unbound, resulting in a eigenfrequency of zero for the surge, sway, heave, roll, pitch and yaw. Once the effect of hydrostatic stiffness is added we should see the heave, roll and pitch to have values above zero. The 4 non-zero values represent the bending modes of the structure. These are there due to the flexibility of the structure itself.
The last part of the 'dry' solution is to find the 'dry' modal mass and 'dry' modal stiffness matrices. These matrices are calculated by combining the eigen vectors and the mass/stiffness matrix as shown in the equation below.

$$\begin{aligned} (\Phi)^T * \mathbf{M}^{str} * \Phi = M_{modal} \\ (\Phi)^T * \mathbf{K}^{str} * \Phi = K_{modal} \end{aligned} \tag{3.11}$$

The value in these matrices represent to which degree the mass/stiffness, that is present within the structural model, contributes to each of the bending modes. More importantly by creating these modal matrices we will be able to calculate the 'wet' eigenfreqency without having to involve the whole structural analysis. For the model these matrices have the following values*.

Location	1	2	3	4	5	6	7	8	9	10
Mass[kg]	14.29	4.987	4.896	3.738	7.368	4.009	5.098	4.035	5.390	2.979

Table 3.6: Modal mass of each mode shape

Location	1	2	3	4	5	6	7	8	9	10
Stiffness[kN/m]	0	0	0	0	0	0	81.0	85.8	302.8	207.7

Table 3.7: Modal stiffness for each mode shape

*Both matrices are diagonal matrices.

3.2.2. 3D hydrodynamic model

Due to the different needs of the structural and hydrodynamic analysis two different meshes were required. The difference being found in the parts of the scale model that needs to be included, compared to the mesh of the structural model the Mesh of the hydrodynamical model was also hollowed out and cut down to the waterline. This had a height of 5.83 [cm]. The reason for doing so was because of the use of a boundary element method (BEM) which doesn't require either the internal structure or the above waterline skin. This means that the eigenvector displacement needs to be translated to the new mesh in order to use the eigenmodes in the hydrodynamic simulations. For each of the flexural modes the displacement is found for each point with Φ_x, Φ_y, Φ_z from the dry eigen vectors. These are then plotted against the coordinates of the new mesh. Interpolation is used to determine the correct displacement for the 'wet' mesh.

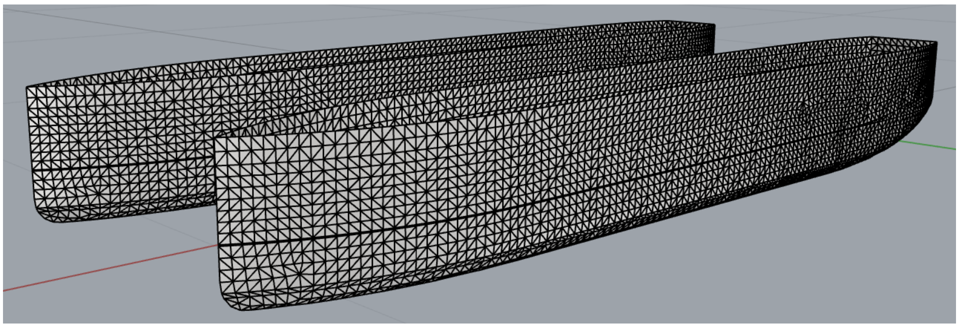

Figure 3.11: Hydro dynamic mesh used with BEM solve

In addition to the displacement of the mesh from the structural deformation, it was also assumed that for the rigid motion the model is undergoing small oscillations in each of the 6 degrees of freedom. The BEM is used to solve the values of the added mass matrix and the hydrostatic- and gravitation-stiffness which are the solutions of the radiation problem with the following equation:

$$A_{ij} - \frac{i}{\omega} B_{ij} = \rho \iint_S n_i \varphi_j dS \tag{3.12}$$

Where A_{ij} in this equation is a component of the added mass and B_{ij} is the hydrodynamic dampening matrix. The n_i is the normal vector of the skin which is used together with φ, which is the mode shape together with a participation factor for the wave excitation frequency of ω. This means that each frequency has its own mass matrix which will be addressed further on. The BEM calculates the values of B_{ij} with the following empirical relationship.

$$B_{ij} = 2\zeta \sqrt{(M_{ij} + A_{ij}(\omega^{wet}))(C_{ij} + k_{ij})} \tag{3.13}$$

For i = j = 3,4,5,6,7,...,N where $A_{ij}(\omega^{wet})$ is the added mass for the modes 3,4,5,6,..,N that correspond to the wet natural frequencies and ζ is the damping ratio. Lastly C_{ij} are the coefficients of the generalized hydrostatic-gravitational stiffness matrix which are given by the following equation.

$$C_{ij} = \rho_{water} g \iint (n_j(w_i + d_r D_i))ds + g \iiint \rho_{structure}(u_j \frac{\delta w_i}{\delta x} + v_j \frac{\delta w_i}{\delta y} + w_j \frac{\delta w_i}{\delta z}) \tag{3.14}$$

This consist of a hydrostatic and gravitational part. The u,w,v in this equation are the displacement degrees of freedom for the wet eigenmodes, while D_r and D_i are the draft of the model and the divergence of the displacement vector. With all of these matrices defined it is possible to solve the forces present in the system in the same way as equation 3.9 which then looks as follows.

$$[-\omega^2(M_{ij} + A_{ij}) + i\omega(B_{ij}) + (C_{ij} + K_{ij})]\mathbf{U}_{wet} = F_i \tag{3.15}$$

This formula can be used to find the wet eigenfrequencies and eigenvectors based upon the 'wet' model.

3.2.3. The iterative procedure

With the procedure described above we are able to make a first guess at the wet eigenfrequencies, but due to the frequency dependency of the added mass matrix, solving these equations is only the first step. In order to solve this problem a iterative procedure was used whereby each mode was solved individually with each cycle generating it's own mass matrix, stiffness matrix and wet eigenmodes. The maximum amount of iterations was set to 1000, while the final tolerance was set to 0.001 [rad/s] for each eigenfrequency. The full process is shown in the figure below.

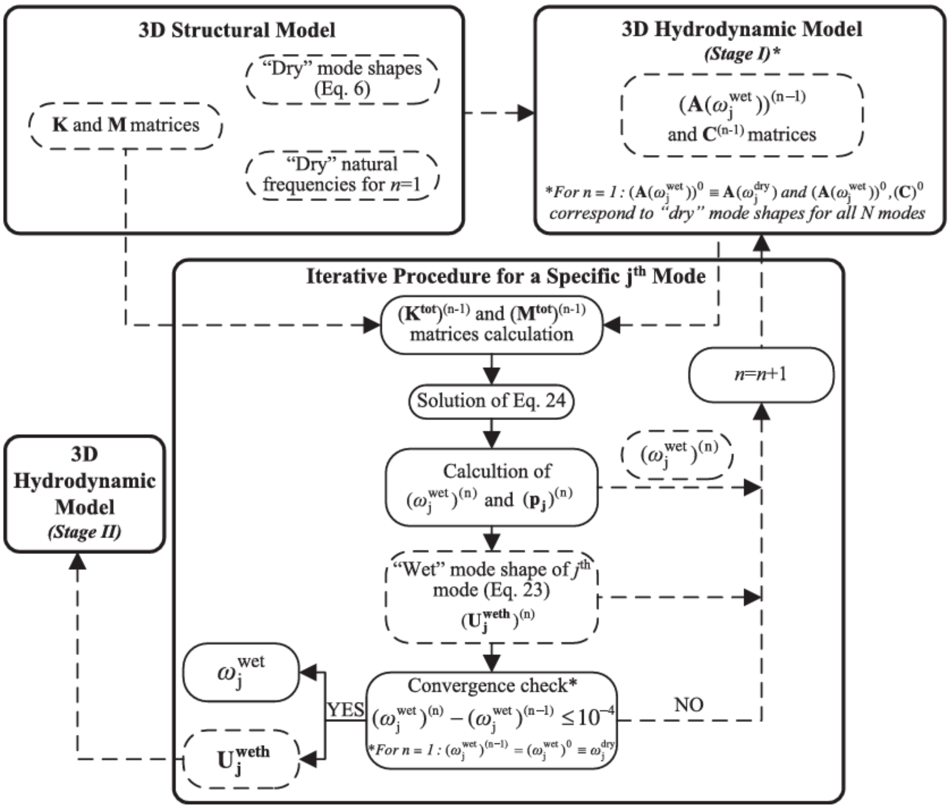

Figure 3.12: Diagram of used procedure as found it [34]

In addition to the above discussed, the paper by Loukogeorgaki [34] also went into the use of these wet eigenmodes in the prediction of the effectiveness of floating barriers. This is not something we made use of and therefore Stage II of the hydrodynamical model is left out.

With this method the following 'wet' eigenfrequencies were found for the different mode shapes at a wave frequency of 28 rad/s.

Mode	rigid-1	rigid-2	rigid-3	pitch	roll	heave	flex-1	flex-2	flex-3	flex-4
Freq[Hz]	0	0	0	0.68	0.8	1.71	17.66	26.64	38.59	48.22

Table 3.8: 'Wet' eigen frequencies of model

One last check needed to be preformed before these values could be used. Because of the way that the added masses were added to the modal mass matrix there is no way to know if the 'dry' eigenmode frequency is the same 'wet' eigenfrequency, as the mathematical operation that determines the outcome has no way of keeping track of the mode shape. It was decided to take the diagonal part of the total mass matrix and the diagonal part of the total stiffness matrix and putting them in the following formula.

$$\omega_i = \sqrt{\frac{K_{ii}}{M_{ii}}} \tag{3.16}$$

Here it was found that no flip had occurred for any of the frequencies. It should be noted that this method ignores the non-diagonal parts of the added mass and stiffness matrices. A better way of checking would be to directly incorporate the hydrodynamic effect into the FEM but this is extremely costly in computational power.

One way to validate the results from the BEM is to check the values for the 'wet' rigid-6 frequencies which in our case is the heave frequency. One can check these values by comparing the ship to a simple 1 degree of freedom mass spring system. In such a system one can predict the natural heave frequency with the formula below:

$$\omega = \sqrt{\frac{K}{M}} = \sqrt{\frac{\rho * A_{wl} * g}{\Delta * \rho}} \approx \sqrt{\frac{9.81 * 0.248}{0.0146}} = 2.054[Hz] \tag{3.17}$$

This is higher then the predicted value from the BEM but it also doesn't include the hydrodynamic dampening or added mass.

3.3. Conclusion

The purpose of this chapter was to demonstrate how the material properties gathered in Chapter 2 were applied to the numerical model created by A. Keser [2]. This was achieved by illustrating how the identified materials were rotated to align with different sections of the material model. Subsequently, the ANSYS ACP Pre module was employed to predict the behaviour of the model's various transverse components using laminate theory. Additionally, an epoxy layer was included in the numerical model to represent the layer applied to the physical model to prevent water ingress.

To incorporate the effect of the surrounding water on the numerical model, a boundary element method (BEM) was used to calculate the added mass and stiffness matrices for each mode shape. The diagonal entries of the total mass and stiffness matrices were then utilized to determine the eigenfrequencies and assess whether the added mass influenced the sequence of the mode shapes.

However, the modified model retains certain shortcomings and limitations. Assigning orthotropic material values requires a coordinate system. Initially, the model had a single coordinate system coinciding with the global system. To accommodate the different sections of the model, seven additional coordinate systems were introduced. The xz-plane system was used for vertical surfaces in that plane, the xy-plane system was used for horizontal surface such as decks and floors. The remaining six coordinate systems corresponded to curved sections of the structure, including the four bulges and the curvature around the wet deck. These coordinate systems were placed at the centre of curvature for their respective sections. For future work, a coordinate system that follows the surface geometry more closely could improve accuracy.

Another limitation lies in the method used to incorporate laminate material properties. The orthotropic material approach, rather than laminate theory, omits the coupling between bending and tension typically present in non-symmetrical ply layups. Additionally, the model assumes that the flexural modulus equals the elastic modulus. Future improvements could address these issues by incorporating more accurate material behaviour.

In the next chapter, we will explore how the changes to the numerical model have influenced its dynamic behaviour.

4

Response and comparison

In this chapter we will be discussing the impact of the different material properties upon the dynamic response. First we will look at the impact of the orthotropic behaviour of the model compared to an isotropic response. Next we will look at the effect of epoxy upon a isotropic model and finally we will compare the completed model to the measurements made by M. Katsouros [35]

4.1. Isotropic response

As with any good comparison the first step is to set up a base line against which all others will be compared. In our case this baseline scenario is the isotropic material model. This model will use the Young's modulus of the vertical direction as this is seen as the main printing direction. This gives the following material values for the plot.

E [Pa]	ν [-]	G [Pa]
1.37e9	0.38	4.96e8

Table 4.1: Isotropic material values

This gives the following dry and wet eigenfrequencies.

Mode	surge	sway	yaw	pitch	roll	heave	flex-1	flex-2	flex-3	flex-4
Freq[Hz]	0	0	0	0	0	0	23.443	25.865	43.115	48.125

Table 4.2: 'Dry' eigenvalues of isotropic material model

mode	surge	sway	yaw	pitch	roll	heave	flex-1	flex-2	flex-3	flex-4
freq[Hz]	0	0	0	0.681	0.806	1.72	16.08	24.53	36.6	45.32

Table 4.3: 'Wet' eigenvalues of isotropic material model

Each of these eigenfrequencies correspond to an eigenvector. These eigenvectors determine how the structure of the ship is deformed. They will also be used to see to which degree the orthotropic material values have an effect on the shape of these eigenmodes.

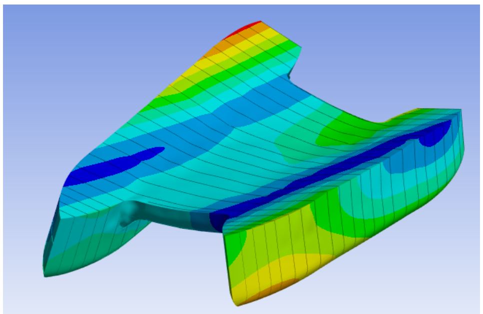

Figure 4.1: 'Dry' mode shape at 23.443 Hz

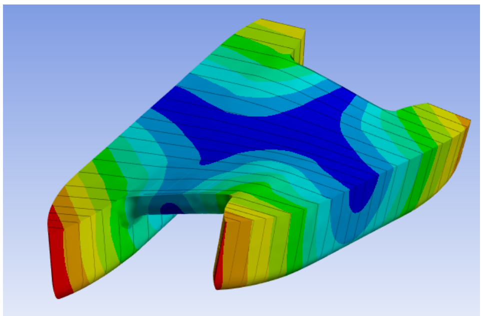

Figure 4.2: 'Dry' mode shape at 25.865 Hz

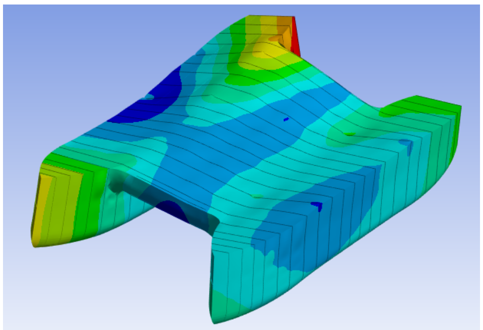

Figure 4.3: 'Dry' mode shape at 43.155 Hz

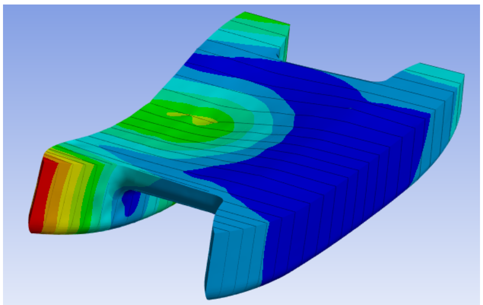

Figure 4.4: 'Dry' mode shape at 48.125 Hz

These eigenvectors will form the baseline behaviour to compare with the other material models. This comparison can be done via a few methods. The first method considered for use was the Modal Assurance Criterion(MAC). This is a mathematical formula used to compare and differentiate different eigenvectors. However it isn't perfect for our proposes. It can compare whole eigenvector for differences but it can't tell where the differences are or even to a sufficient degree how large they are, only that they are present. Hereby turning us away from this particular approach of determining the impact.

The second method, was to imitate the use of Strain gauges within the model. This involved scaling all the displacement to have the same amplitude across the different material values and then determining the difference in strain on predetermined locations. This method would allow for a qualitative comparison of the difference in mode shapes, and would allow for a complete comparison of multiple material models instead of individual comparison. This would be required when comparing strain in the total structure. However this does reduce the degree to which the difference in response are visible to those points, which if chosen poorly could show reduced impact. So a middle ground was sought.

This middle ground was found in the displacement of the main deck. As a 2D structure it would allow for a large area to be compared and the results easily displayed without having to inspect multiple layers. Additionally the physical model was also created to measured the deformation of the model with a digital imaging camera (DIC) setup through a spotted pattern on the main deck. This does mean that that we wont see the effect of the water upon the eigenvectors, as this deck isn't part of the mesh of the BEM.

4.2. Orthotropic response

The first material properties to be investigated are the orthotropic properties. In order to determine the effect of different levels of orthotropic behaviour the material model for the ship will be created over a range of different Young's moduli and Shear moduli. For this part the Poisson ratios will be kept constant. According to this setup the following material values were tested.

E [Pa]	ν	G[pa]
1.37e9-1.78e9 [Pa]	0.33 [-]	4.96e8-6.45e8 [Pa]

Table 4.4: Material value range

All three youngs moduli were varied across this range with a 5 steps. Creating a total of 125 points of measurement for the orthotropic behaviour. This behaviour was then plotted with a scatter plot in 3D space. Finally all Young's moduli were expressed as a fraction of isotropic E3 to create a non dimensional view of the orthtropic behaviour

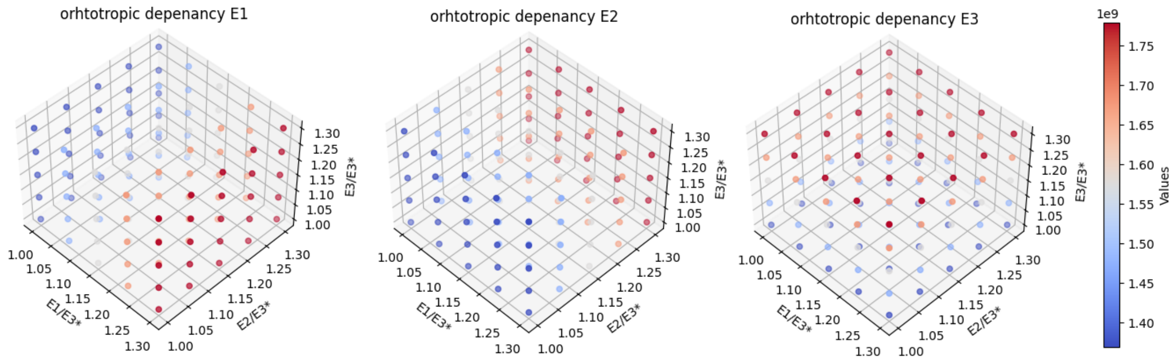

Figure 4.5: Spread of Young's moduli

The figure above shows the different Young's moduli for each degree of orthotropic behaviour. E_1, E_2 and E_3 are the modulus in the longitudinal, transversal and vertical direction respectively. Or in other words E_1 is along the hull vertically, E_2 is into the skin of the hull, and E_3 is along the length of the model.

4.2.1. First mode

The first eigenmode can be seen in figure 4.1 and can be roughly described as a two node bending of the model with the node lines being across the deck, These are indicated by the two blue lines seen in the figure. Using the different material values from figure 4.5 the following figure was made for the change in the eigenfrequencies.

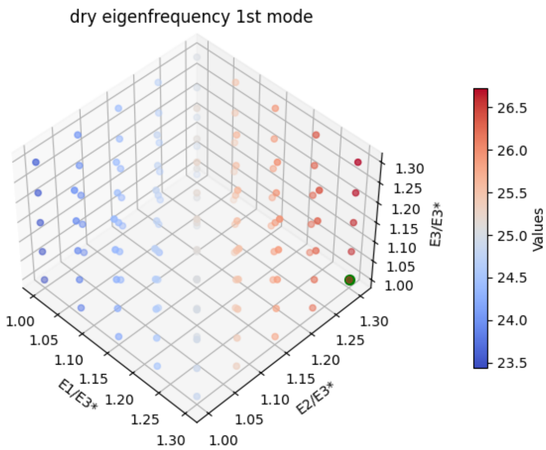

Figure 4.6: 'Dry'&'wet' eigenfrequency across orthotropic range

looking at the Figures 4.6, one can see the behaviour of the eigenfrequency over the different material values. For the first mode it appears that the eigenfrequency is mostly determined by the behaviour of E1 and E2 which could be expected as the frequency would mostly be influenced by the transverse stiffness of the model. Which is made up of the bulkhead and horizontal decks, these in turn have there stiffness in that direction determined by E_2 and E_1 respectively. Additionally the Green dot visible at the right corner indicate the measured orthtropic relationship.

Next we will look at the change in the eigenmode that corresponds to the different extremes in Young's moduli for each directions. These are shown below.

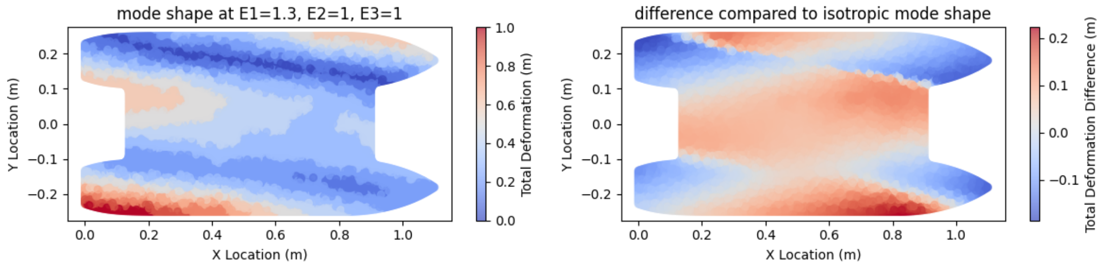

Figure 4.7: Effect upon eigenmode 1 from increasing E_1

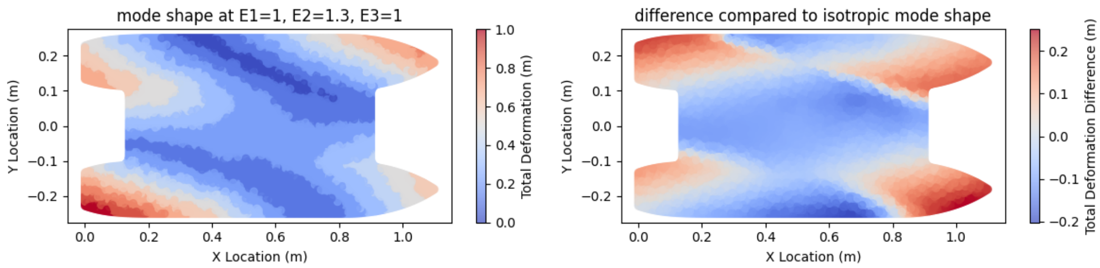

Figure 4.8: Effect upon eigenmode 1 from increasing E_2

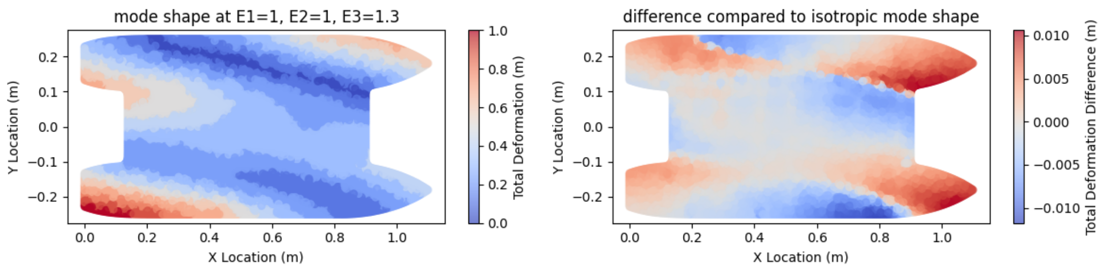

Figure 4.9: Effect upon eigenmode 1 from increasing E_3

Figures 4.7 to 4.9 show the shape of the eigenmode in the deck and the difference in total displacement of the eigenmodes for the different axis of orthotropic behaviour with the isotropic eigenmode being used as the point of comparison. Looking at the total deformation difference we can see that E1 and E2, compared to the E3 seem to have the smallest amount of effect upon the mode shape reflecting it's impact upon the eigenfrequencies. In comparison E1 and E2 seem to shift the node lines in an anti clockwise and clockwise direction respectively. It appears than when both E1 and E2 are increased, the changes in the mode shape seem to cancel each other out as can be seen in the figure below.

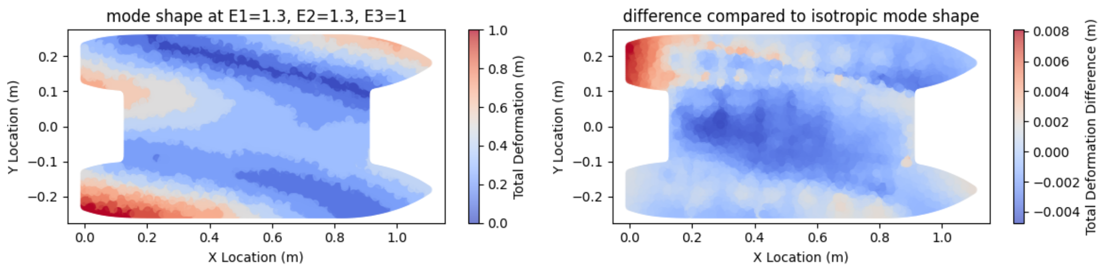

Figure 4.10: Effect upon eigenmode 1 from increasing $E_1 \& E_2$

This means this mode shape is not effected by the orthotropic behaviour of the 3d printed material to any large degree.

4.2.2. Second mode

The second eigenmode can be seen in figure 4.2 and can be described as a torsional bending mode of the model. This eigenmode is mostly present in the deck of the model, with the two hulls remaining undeformed. Plotting the dry eigenmodes, the following frequencies were found across the material range.

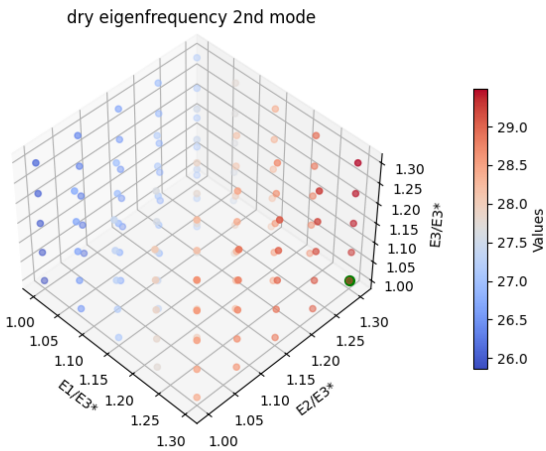

Figure 4.11: 'Dry' eigenfrequency across orthotropic range

Similarly to the first mode the second mode doesn't seem to be effected by changes to the E3. Compared to E2, E1 is slightly more important compared tot the first mode. The reason for this could be the method of the shear modulus determination. With both G12 an G13 being determined by E1 and G23 being derived from E2. This would also explain the limited effect of E3. Next we will look at the effect upon the mode shape.

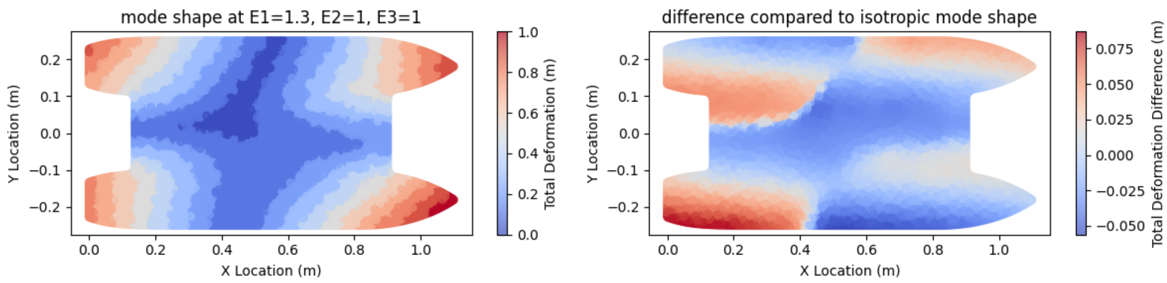

Figure 4.12: Effect upon eigenmode 2 from increasing E_1

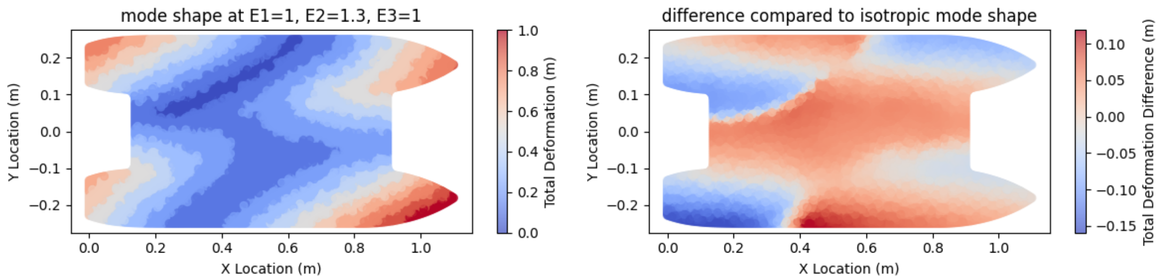

Figure 4.13: Effect upon eigenmode 2 from increasing E_2

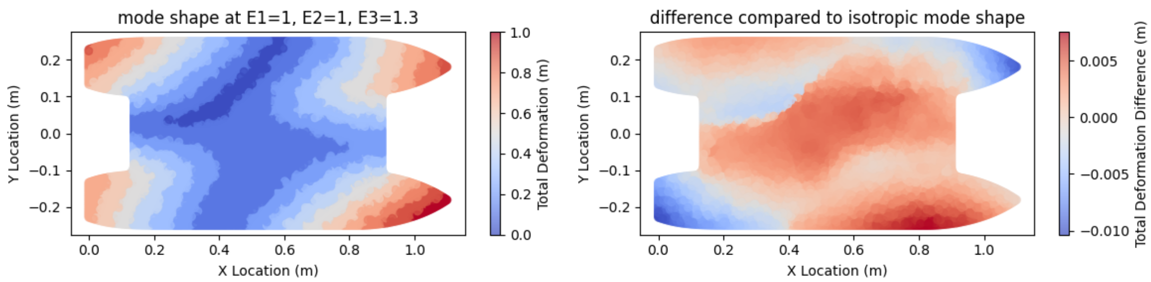

Figure 4.14: Effect upon eigenmode 2 from increasing E_3

Figures 4.12 to 4.14 show the differences in the eigenmodes for the second mode shape. Compared to the first mode shape the overall level of difference is lower with the maximal difference being only 0.15. With E3 showing the smallest amount of difference overall. The effect of changing E2 is more apparent. Compared to the first mode, it appears that instead of torsional behaviour being measured, the mode-shape has shifted to bending behaviour with two node lines. With E1 seemingly having the opposite effect.

4.2.3. Third mode

The third eigenmode of the model [seen in figure 4.3] is best defined as a 3 point bending mode, with each pontoon and the middle of the deck being the nodes for the bending movement. Additionally there is also a small amount of bending present in the starboard pontoon. Using the orthotropic material values the following dependency was found.

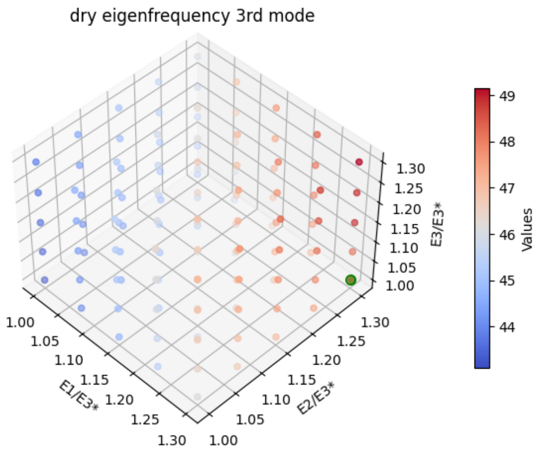

Figure 4.15: 'Dry' eigenfrequency across orthotropic range

For the third mode the third Young's modulus does appear to have a impact upon the response slightly increasing it. But the overall behaviour is still determined by E1 and E2. Because they form the cross deck stiffness of the structure. The effect of the third direction seems to come from the bending of the starboard pontoon.

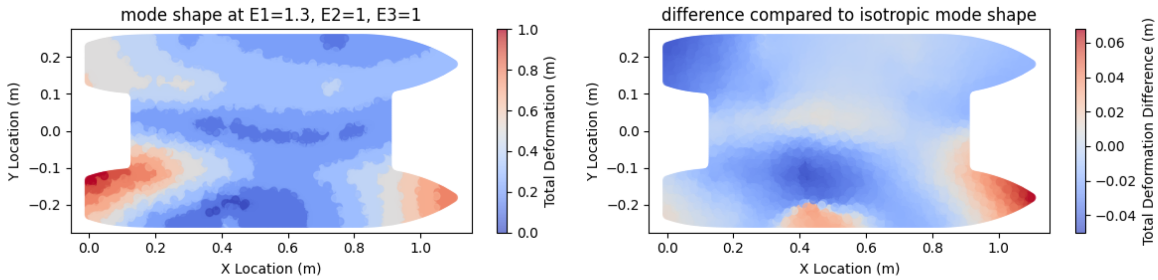

Figure 4.16: Effect upon eigenmode 3 from increasing E_1

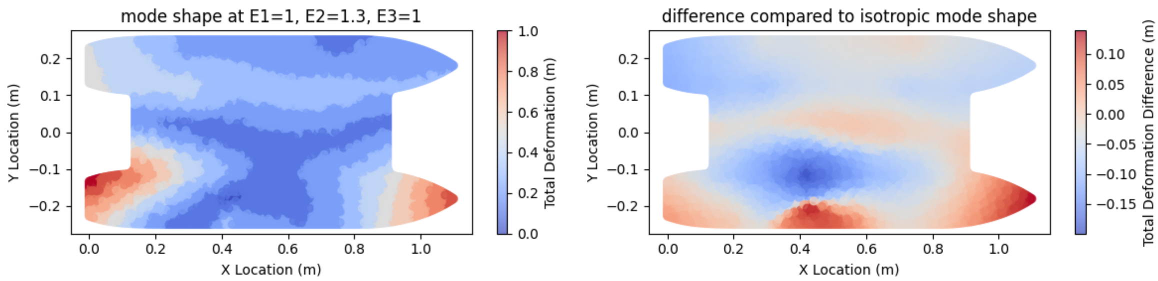

Figure 4.17: Effect upon eigenmode 3 from increasing E_2

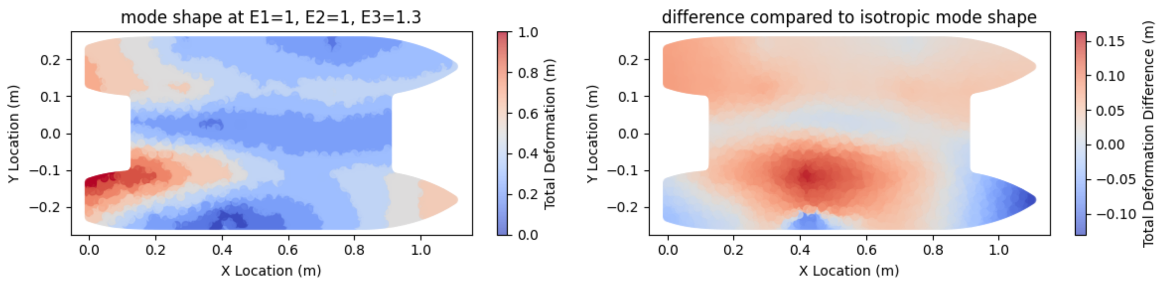

Figure 4.18: Effect upon eigenmode 3 from increasing E_3

For the third mode it appears that E1 has the smallest effect upon the mode shape mostly increasing the presences of the bending behaviour in the pontoon. Additionally it appears that the amplitude of the bending in the rest of the structure is largely decreased. E2 seems to have a similair effect, but with more emphasize upon the increase of the bending behaviour, compared to the decrease in the overall bending. Finally a increase in E3 seems to reduce the bending behaviour of the starboard hull while increasing the amplitude of the 3 point bending behaviour of the rest of the structure.

4.2.4. Fourth mode

The fourth eigenmode of the model is seen in figure 4.4. It consists of a two node bending of the starboard pontoon. This mode fully shows the bending present in mode three without the torsional component. This also means that the left hull and the working deck are largely undeformed. Using the different material values the following figure is made.

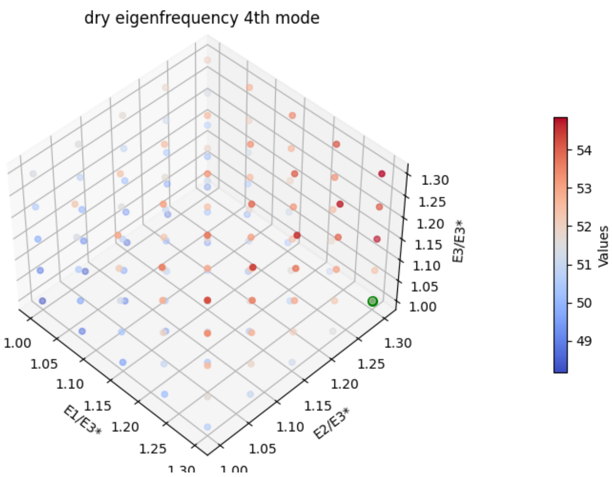

Figure 4.19: 'Dry' eigenfrequency across orthotropic range

Looking at the mode shape one would expect that E3 would dominate this mode shape, and out of all the mode-shapes that are of interest it does show the clearest dependency upon it. However it appears that E1 also effects the frequency of this mode to a similar degree. E2 doesn't appear to have any effect on this mode. This is in contrast to the mode shapes in which E2 causes the largest shift compared to the other two, as can be seen below.

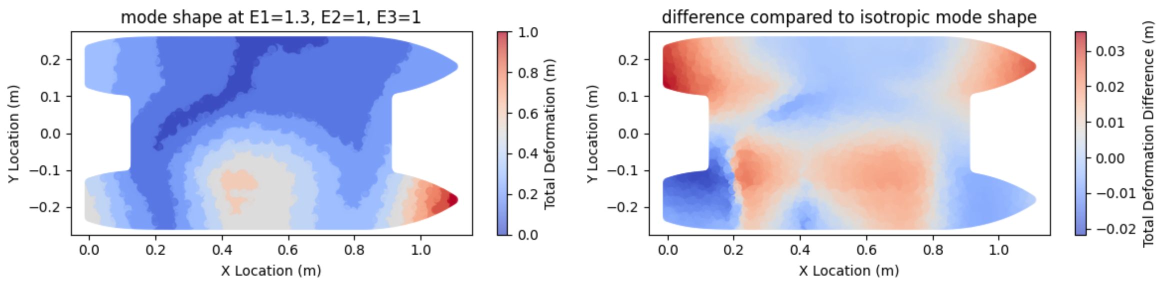

Figure 4.20: Effect upon eigenmode 4 from increasing E_1

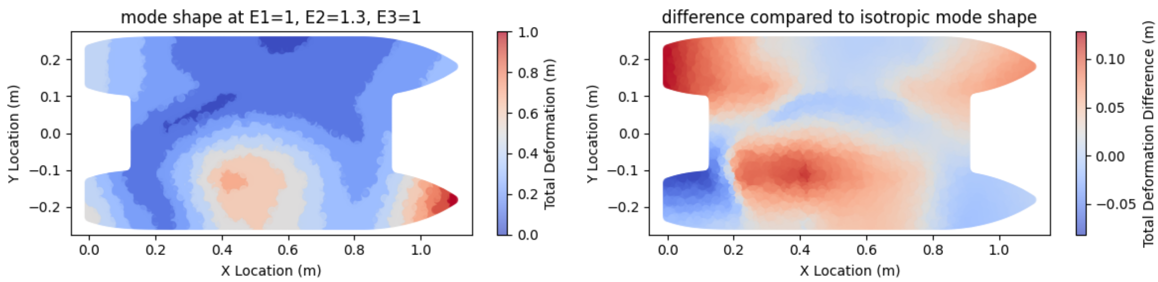

Figure 4.21: Effect upon eigenmode 4 from increasing E_2

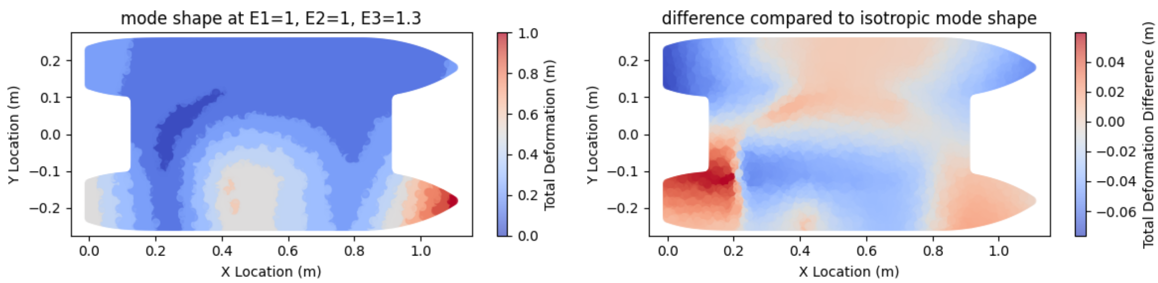

Figure 4.22: Effect upon eigenmode 4 from increasing E_3

When looking at the mode shapes one might at first glance think that an increase of the E3 shows an increase in the bending behaviour of the pontoon. This is not the case however. Since all mode shapes were scaled to have a maximum distortion of 1, and the point of the pontoon has the largest displacement. A decrease in bending is visible as a relative increase behind the point of the pontoon, which itself has an increase of zero. This has caused the relative values behind the point too increase, which is visible in the figure as the red colour. With the opposite effect being visible with the increase of E1 and E2.

From all the different plots above we can conclude the following. While the eigenfrequencies do change across the orthotropic range, there isn't any material value for which they switch in order. Secondly when looking at the mode shapes we can say the following: when a stiffness in any particular direction is below the average of all directions the mode shapes associated with that direction will be more pronounced and when the stiffness is above the average that behaviour is suppressed, when compared to a isotropic material.

4.3. Epoxy

With the impact of the orthotropic behaviour now characterised our next step is to look at the influence of the epoxy layer upon the model. For this we will be comparing the dry, wet and eigenmode of the

model with and without a epoxy layer.
The material values of this comparison are as follows.

Table 4.5: Material values for impact epoxy

	E [Pa]	nu	G [Pa]
PETG	1.37e9	0.38	4.96e8
Epoxy	2.6e9	0.33	9.77e8

These material values were put into the model which gave the following eigenfrequencies which we can compare to the model without epoxy.

Table 4.6: Results of impact epoxy

	1st	2nd	3rd	4th
Dry	23.443	25.865	43.115	48.125
Dry + epoxy	24.021	26.679	44.052	49.495

Table 4.7: Wet eigenvalues of isotropic material model

Mode	surge	sway	yaw	pitch	roll	heave	flex-1	flex-2	flex-3	flex-4
Wet [Hz]	0	0	0	0.68	0.81	1.78	16.08	24.53	36.6	45.32
Wet + epoxy	0	0	0	0.68	0.81	1.78	16.79	25.19	37.52	46.44

For both the wet and the dry frequencies it appears that the adding of the epoxy has increased the measured frequency as one would expect. The average increase seems to be around 2.9 % when compared to the isotropic case. With an average increase of the measured frequency of 0.8805 [Hz]. It should be noted however that is the case for the scale model. When scaling back up to the predicted response for the full model this becomes an average increase of 0.068 [Hz] when compared to the isotropic case.

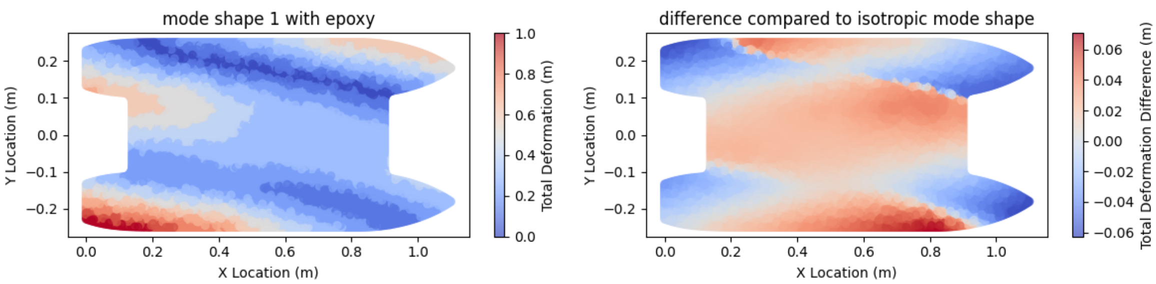

Figure 4.23: Effect upon eigenmode 1 from epoxy

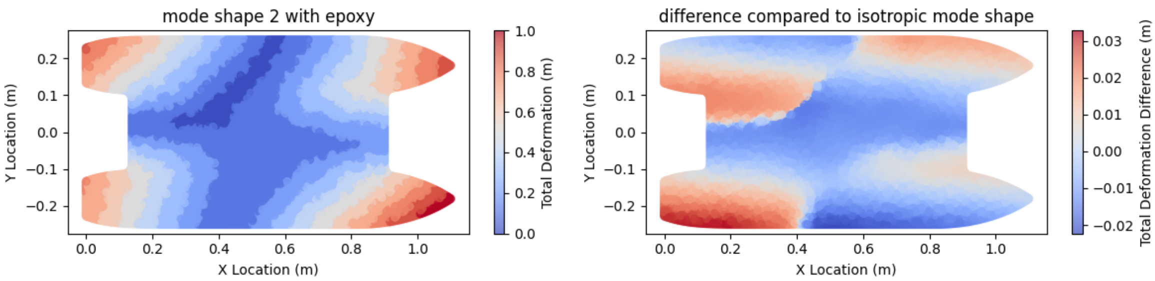

Figure 4.24: Effect upon eigenmode 2 from epoxy

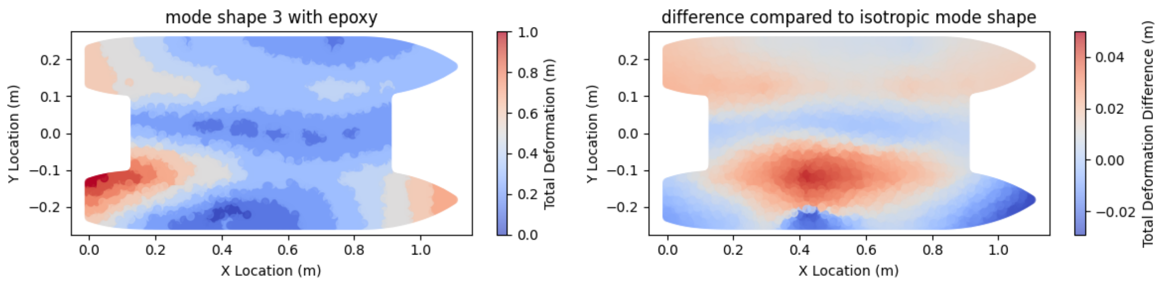

Figure 4.25: Effect upon eigenmode 3 from epoxy

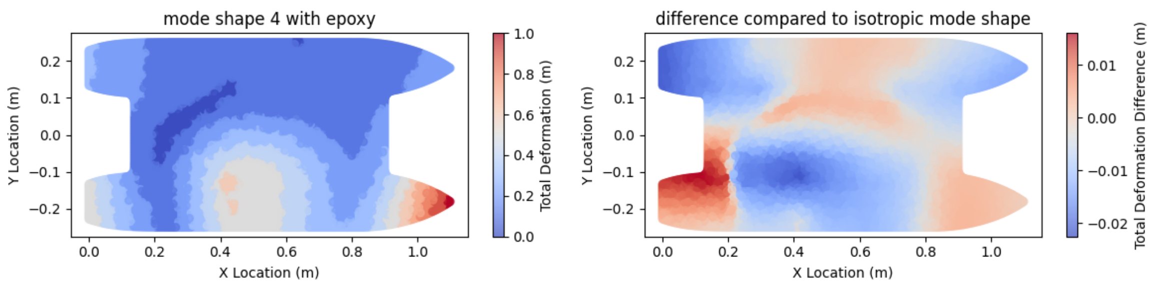

Figure 4.26: Effect upon eigenmode 4 from epoxy

Compared to the orthotropic response it seems that the epoxy has a limited effect upon the mode shapes. With the largest measured difference being 0.06, the mode shapes themselves are remarkably similair to the behaviour of the orthtropic changes. With the first mode being similar to an increase in E1, the second E1, the third E3 and the fourth E3. This can be explained with the way the epoxy was applied upon the outer skin. Where it contributes to the stiffness in the directions of E1 and E3. With E2 only being relevant for the bulkheads and even then only the rear most bulkhead had epoxy applied to it. It was observed that the change of each mode shape seems to be based upon it's dependency of orthotropic behaviour. The first and second mode shape have a larger change corresponding to E1 and the third and fourth mode have a larger change to their amplitude for a increase in E3 compared to E1.

4.4. Full material model with epoxy

With the degree of orthotropic and epoxy covered behaviour now determined, we can look at the effect with the complete elastic model including the frequency dependency found in chapter 2. This was done with a manual iterative method. This involved calculating the wet natural frequency of any mode followed by inputting the corresponding material properties found for the next round. Using this method the following wet frequencies were found. Because of the orthotropic behaviour it was decided that in addition to the isotropic case based upon the measured value for E3*, we will also compare the frequency with a similarly orthotropic model for a better comparison for the frequency dependent behaviour.

Table 4.8: Change in predicted frequency due to frequency dependant material properties in 'wet' model

frequency	1st	2nd	3rd	4th
Experimental	18	21	-	40
Isotropic dry	25.507	28.095	46.358	50.657
Isotropic wet	16.08	24.53	36.6	45.32
Isotropic+epoxy wet	16.79	25.19	37.52	46.44
Orthotropic wet	18.22	27.76	39.67	49.52
Complete 'wet'	18.23	27.64	39.51	49.3

Looking at the frequency, we can see that compared tot the isotropic model the frequency overall increased. However with the addition of the orthotropic comparison it becomes clear that this is caused by the increase in E1 and E2. The frequency dependency does appear to have an effect. Changing the measured frequency to a lower value when compared to the static frequency of the same orthogonal measurement. It appears that even with the steep frequency dependency the small frequency range only causes a difference by 0.22 [Hz] for the highest mode. The mode shape will also be compared.

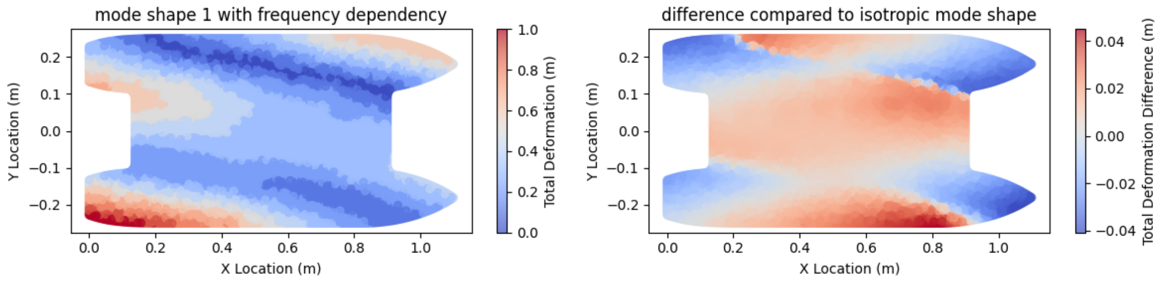

Figure 4.27: Effect upon eigenmode 1 from epoxy

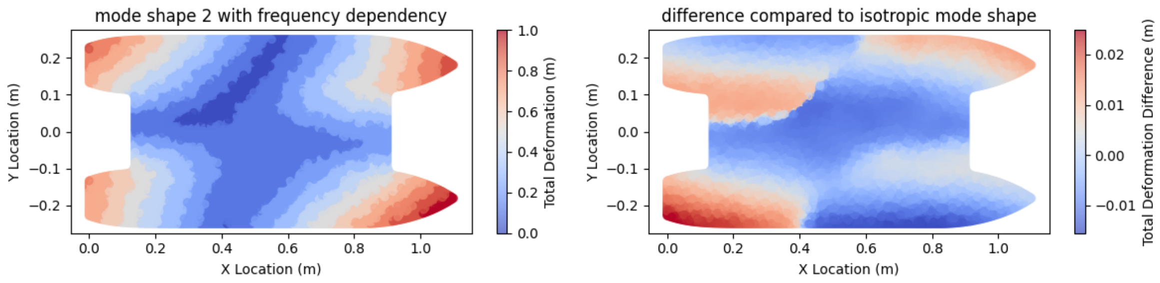

Figure 4.28: Effect upon eigenmode 2 from epoxy

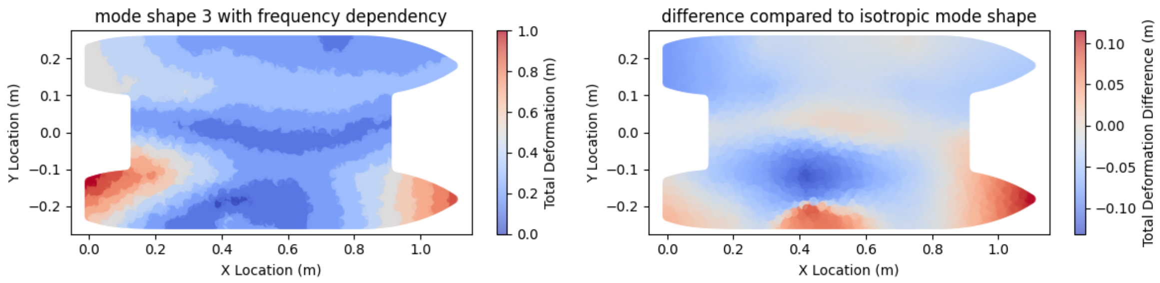

Figure 4.29: Effect upon eigenmode 3 from epoxy

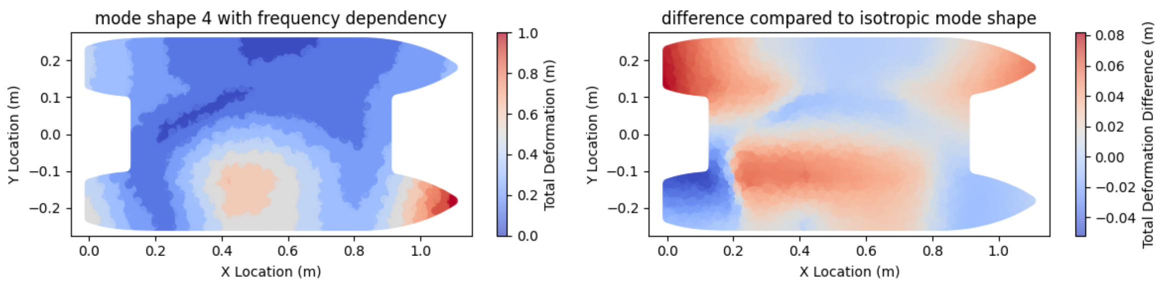

Figure 4.30: Effect upon eigenmode 4 from epoxy

The mode shape for the frequency dependent model does differ from the basic model but this seems to be due to the orthtropic behaviour and the change in frequency. With all modes following largely the same behaviour as the increase in E1.

4.4.1. Compared to physical model experimental testing

With the model complete we can compare it to the numerical predictions with the measured values for M. katsouros [35], which were acquired by hammer testing in water.

Table 4.9 shows the different predicted modes of the numerical model and the measured result from the in water testing. The 1st, 2nd and 4th mode shapes of the numerical model were matched to the 1st, 2nd and 3rd mode shapes respectively of the physical measurements. With the predicted 3rd modeshape not being found. This was done based upon the assignment of [35]. This is in contrast to the finding of A. Keser [2] where the first and second mode shapes of the experimental results were reversed. With the second mode shape having a frequency of 20 and the first having a frequency of 22.

Initially it was thought that the observed differences between the numerical model and the experimental model could be attributed to several factors. Including: the presence of epoxy in the experimental model, the effect of the added mass, variations in transverse stiffness and the exact placement of weights within the model.

Having now addressed several of these unknown factors it can be concluded that the difference in behaviour is not caused by the addition of epoxy layer or the inclusion of hydro dynamic effects. Additionally the effect of frequency dependency for the interested frequency range is also limited. This would mean that the remaining unknown factors consist of the precise placement of the weights in the model and the transversal thicknesses of the bulkheads and the influence of the coupling between the bending and tension of 3D printed laminates.

mode shape		frequencies	
numerical	physical	numerical	physical
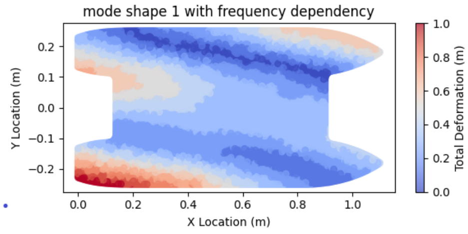	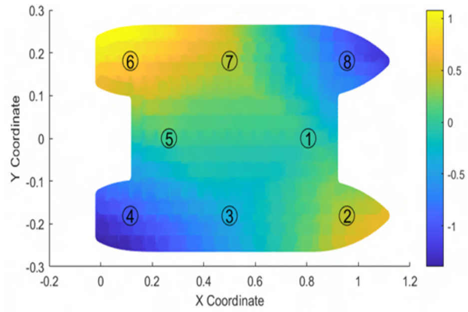	18.23	18
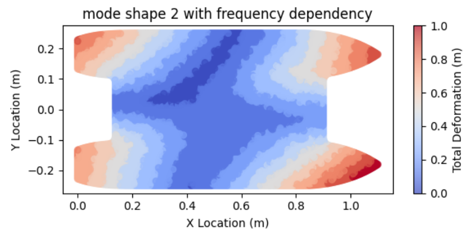	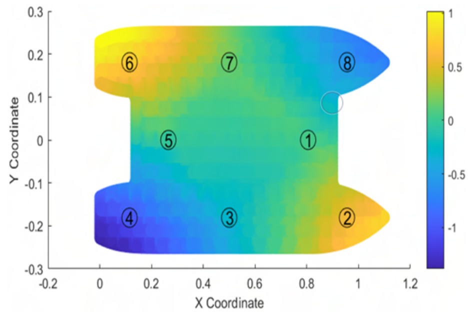	27.64	21
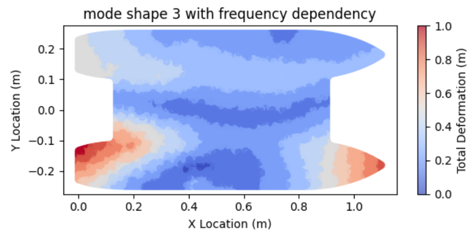		39.51	-
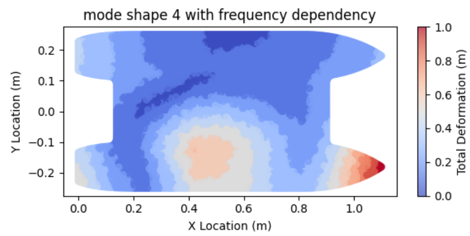	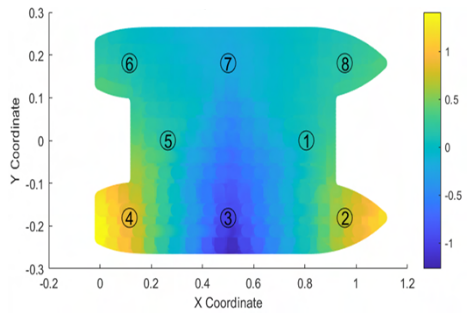	49.3	40

Table 4.9: Table comparison between numerically model and fully elastic model with accelerometers in water as found in [35]

4.4.2. Recommendations

With the influence upon the eigenfrequencies and eigenmodes of the different material properties now determined, we will quickly go over some possible counter measures in design and construction methods that could be attempted to reduce the influence.

Orthotropic behavior: From the material analysis it appear that the relationship between E1, E2 and E3 for the interested range is 1,1,0.8 which does effect the measured eigenfrequency here. With the overall dominance of the first Young's modulus it is advised to use that modulus for the design of the model. One possible way of solving this problem is to vary the printer settings in search of a reduced orthotropic behaviour.

Epoxy coating: With the influence of the epoxy on the structure now understood, two primary options emerge to mitigate its effects. The first option is to explore alternative sealing methods, while the second involves reducing the epoxy's thickness without compromising water tightness. The different sealing approaches could consist of melting the outside of the model either with heat or possibly by chemically dissolving the outermost layer. Both approaches pose there own difficulties, Heating thin walls can be difficult as melting thought the thin walls would be a significant risk. The chemical approach would in-tail vaporizing ethyl acetate and placing the whole model in this vapour. Another option is to apply the epoxy with an airbrush, resulting in a thinner coat. However, it remains uncertain whether an airbrushed epoxy coating would achieve adequate water tightness.

frequency dependency: While it is seen that the frequency dependency that is measured was only for a small frequency range, it's limited effect indicated that with the expected frequency range one would not have to compensate for the shift.

4.5. Conclusion

The goal of this chapter was to discuss the impact of various material properties associated with 3D-printed PETG using the updated numerical model.

The first material property investigated was the orthotropic behaviour, where different degrees of orthotropy were compared. It was found that while an increase in Young's modulus suppresses specific mode shapes within a given mode, the orthotropic behaviour does not alter the sequence of these mode shapes.

Additionally, the effect of adding a watertight epoxy layer to the outer surface of the structure was examined. This layer was shown to increase the stiffness of the outer layers, resulting in a higher measured frequency, while not significantly influencing the mode shapes.

Finally, the previous material properties were combined with the frequency dependency measured in Chapter 2 to assess the shift in frequency for the targeted mode shape. This analysis revealed a frequency shift of -0.22 Hz for the fourth mode when compared to the static material properties.

While the new model accounted for these material properties, There is still a significant difference between the measured values and those predicted by the model namely there is a increasing error at higher frequencies. It is suspected that this is caused by the material values of the PETG being to high. for the model itself there are still points of improvement: The unknown thicknesses of the transverse sections, the coupling between tension and shear, and the precise placement of the weights as likely causes of the observed difference. Together with the possible material value difference.

5 Conclusion

The primary aim of this research was to investigate the dynamic material properties of 3D-printed PETG and understand how these properties influence the design of fully elastic models.

To obtain the material values for this study, shaker experiments were conducted on PETG specimens. These tests revealed that the 3D-printed PETG exhibits both orthotropic and frequency-dependent behaviour. However, the shaker method proved inadequate for capturing the continuous frequency dependency accurately, highlighting the need for a more suitable testing approach. For future studies a setup utilizing guided waves is recommended, as it would likely provide a clearer picture of the frequency-dependent properties across a broader frequency range.

The determined material properties were integrated into a numerical model, with PETG treated as an orthotropic material. Additionally, the model accounted for the impact of an epoxy layer applied to the physical structure by incorporating laminate theory to simulate this layer's influence. To capture the hydrodynamic effects of the water surrounding the model, a Boundary Element Method (BEM) was employed, providing the necessary added mass and hydrodynamic stiffness matrices.

The updated numerical model was subsequently used to assess the impact of the various material models. The results indicated that none of the examined material properties led to differences when compared to the behaviour observed in the physical model. Furthermore, the frequency dependency within the examined range was found to have only a limited effect, suggesting it may not be as critical as initially anticipated for the first four eigenfrequencies of this elastic model.

It was also observed that the orthotropic behaviour of the PETG and the presence of the epoxy layer had measurable effects on the eigenfrequencies, indicating that these aspects should be considered carefully in future additively manufactured designs. Specifically, strategies should be developed to minimize the influence of these factors for future designs.

It should be noted that the numerical model as it exists now has certain limitations. Due to the use of an orthotropic material model for the composite sections, it does not account for coupling effects between bending and shear, and the flexural modulus is assumed to be equal to the elastic modulus. Future work could explore modifications to address these limitations, thereby enhancing the model's accuracy and reliability for applications involving complex material behaviour.

6 Recommended research

While this report has addressed some aspects of material behaviour and model accuracy, other subjects remain open for further investigation. Either due to time constraints or them laying outside the scope of this report. These subject can be sorted in the following overall categories: Material determination, numerical model improvement and fabrication adjustments.

Material determination

- Used guided wave upon 3D printed specimen to determine the Young's modulus for a continuous frequency band.
- independent measuring of the different shear moduli with Poisson ratio's.

Numerical model improvement

- Modify the model to include the coupling between bending and torsion of composite sections through the use of the ACP module in ANSYS Mechanical.
- Investigate the changing of behaviour with differing placement of weights within the structure.

Fabrication adjustments

- Investigate the viability of creating a watertight epoxy layer with airbrush or the sealing of outside layers by sculpting tool.
- sealing the outside of the 3D printed structure through chemically dissolving layers
- Investigate if the printing settings can be adjusted to minimize the orthotropic behaviour.

References

[1] P. Saltonstall. “World’s largest 3d-printed boat.” (), [Online]. Available: https://maineboats.com/print/issue-162/university-maine-3dirigo (visited on 02/20/2024).

[2] A. Keser, M. Verdult, H. C. Seyffert, and A. Grammatikopoulos, *The design, production, verification, and calibration of an elastic model of a catamaran for hydroelastic experiments*. Oct. 2023. DOI: 10.3233/pmst230019. [Online]. Available: https://doi.org/10.3233/pmst230019.

[3] A. Grammatikopoulos, “A review of physical flexible ship models used for hydroelastic experiments,” *Marine Structures*, vol. 90, p. 103 436, Jul. 2023. DOI: 10.1016/j.marstruc.2023.103436. [Online]. Available: https://doi.org/10.1016/j.marstruc.2023.103436.

[4] J. Jiao, H. Ren, and C. G. Soares, “A review of large-scale model at-sea measurements for ship hydrodynamics and structural loads,” *Ocean Engineering*, vol. 227, p. 108 863, May 2021. DOI: 10.1016/j.oceaneng.2021.108863. [Online]. Available: https://doi.org/10.1016/j.oceaneng.2021.108863.

[5] I. Senjanović, Š. Malenica, and S. Tomašević, “Hydroelasticity of large container ships,” *Marine Structures*, vol. 22, no. 2, pp. 287–314, Apr. 2009. DOI: 10.1016/j.marstruc.2008.04.002. [Online]. Available: https://doi.org/10.1016/j.marstruc.2008.04.002.

[6] B. Shabani, J. Lavroff, M. R. Davis, D. Holloway, and G. Thomas, “Slam loads and pressures acting on high-speed wave-piercing catamarans in regular waves,” *Marine Structures*, vol. 66, pp. 136–153, Jul. 2019. DOI: 10.1016/j.marstruc.2019.03.007. [Online]. Available: https://doi.org/10.1016/j.marstruc.2019.03.007.

[7] A. Grammatikopoulos, J. Banks, and P. Temarel, “Prediction of the vibratory properties of ship models with realistic structural configurations produced using additive manufacturing,” *Marine Structures*, vol. 73, p. 102 801, Sep. 2020. DOI: 10.1016/j.marstruc.2020.102801. [Online]. Available: https://doi.org/10.1016/j.marstruc.2020.102801.

[8] A. Grammatikopoulos, J. Banks, and P. Temarel, “The design and commissioning of a fully elastic model of a uniform container ship,” *Marine Structures*, vol. 78, p. 103 014, Jul. 2021. DOI: 10.1016/j.marstruc.2021.103014. [Online]. Available: https://doi.org/10.1016/j.marstruc.2021.103014.

[9] S.-H. Ahn, M. Montero, D. Odell, S. Roundy, and P. K. Wright, “Anisotropic material Properties of fused deposition Modeling ABS,” *Rapid Prototyping Journal*, vol. 8, no. 4, pp. 248–257, Oct. 2002. DOI: 10.1108/13552540210441166. [Online]. Available: https://doi.org/10.1108/13552540210441166.

[10] O. A. Mohamed, S. H. Masood, and J. Bhowmik, “Process parameter optimization of viscoelastic properties of FDM manufactured parts using response surface methodology,” *Materials Today: Proceedings*, vol. 4, no. 8, pp. 8250–8259, Jan. 2017. DOI: 10.1016/j.matpr.2017.07.167. [Online]. Available: https://doi.org/10.1016/j.matpr.2017.07.167.

[11] J. L. C. Quintana *et al.*, “Viscoelastic properties of fused filament fabrication parts,” *Additive Manufacturing*, vol. 28, pp. 704–710, Aug. 2019. DOI: 10.1016/j.addma.2019.06.003. [Online]. Available: https://doi.org/10.1016/j.addma.2019.06.003.

[12] J. Chacón, M. Caminero, E. G. Plaza, and P. J. Núñez, “Additive manufacturing of PLA structures using fused deposition modelling: Effect of process parameters on mechanical properties and their optimal selection,” *Materials Design*, vol. 124, pp. 143–157, Jun. 2017. DOI: 10.1016/j.matdes.2017.03.065. [Online]. Available: https://doi.org/10.1016/j.matdes.2017.03.065.

[13] M. Somireddy and A. Czekanski, “Anisotropic material behavior of 3D printed composite structures – Material extrusion additive manufacturing,” *Materials Design*, vol. 195, p. 108 953, Oct. 2020. DOI: 10.1016/j.matdes.2020.108953. [Online]. Available: https://doi.org/10.1016/j.matdes.2020.108953.

[14] Y.-H. Huang and C. Lin, “Measurement of orthotropic material constants and discussion on 3D printing parameters in additive manufacturing,” *Applied sciences*, vol. 12, no. 13, p. 6812, Jul. 2022. DOI: 10.3390/app12136812. [Online]. Available: https://doi.org/10.3390/app12136812.

[15] A. Milovanović *et al.*, “Manufacturing parameter influence on FDM polypropylene tensile properties,” *Journal of Mechanical Science and Technology*, vol. 37, no. 11, pp. 5541–5547, Oct. 2023. DOI: 10.1007/s12206-023-2305-5. [Online]. Available: https://doi.org/10.1007/s12206-023-2305-5.

[16] P. Biswas, S. Guessasma, and J. Li, “Numerical prediction of orthotropic elastic properties of 3D-printed materials using micro-CT and representative volume element,” *Acta Mechanica*, vol. 231, no. 2, pp. 503–516, Nov. 2019. DOI: 10.1007/s00707-019-02544-2. [Online]. Available: https://doi.org/10.1007/s00707-019-02544-2.

[17] L. Sosa-Vivas, J. Gonzalez-Delgado, and G. Torrente, “Experimental and numerical study of orthotropic behavior of 3D printed polylactic acid by material extrusion,” *Progress in additive manufacturing (Online)*, vol. 8, no. 5, pp. 947–959, Dec. 2022. DOI: 10.1007/s40964-022-00369-5. [Online]. Available: https://doi.org/10.1007/s40964-022-00369-5.

[18] J. F. Rodríguez, J. P. Thomas, and J. E. Renaud, “Mechanical behavior of acrylonitrile butadiene styrene fused deposition materials modeling,” *Rapid Prototyping Journal*, vol. 9, no. 4, pp. 219–230, Oct. 2003. DOI: 10.1108/13552540310489604. [Online]. Available: https://doi.org/10.1108/13552540310489604.

[19] R. Zou *et al.*, “Isotropic and anisotropic elasticity and yielding of 3D printed material,” *Composites Part B: Engineering*, vol. 99, pp. 506–513, Aug. 2016. DOI: 10.1016/j.compositesb.2016.06.009. [Online]. Available: https://doi.org/10.1016/j.compositesb.2016.06.009.

[20] T. Yao, Z. Deng, K. Zhang, and S. Li, “A method to predict the ultimate tensile strength of 3D printing polylactic acid (PLA) materials with different printing orientations,” *Composites Part B: Engineering*, vol. 163, pp. 393–402, Apr. 2019. DOI: 10.1016/j.compositesb.2019.01.025. [Online]. Available: https://doi.org/10.1016/j.compositesb.2019.01.025.

[21] S. Dai, Z. C. Deng, Y. J. Yu, K. Zhang, S. H. Wang, and J. Ye, “Orthotropic elastic behaviors and yield strength of fused deposition modeling Materials: Theory and Experiments,” *Polymer Testing*, vol. 87, p. 106 520, Jul. 2020. DOI: 10.1016/j.polymertesting.2020.106520. [Online]. Available: https://doi.org/10.1016/j.polymertesting.2020.106520.

[22] I. M. Daniel and O. Ishai, *Engineering Mechanics of composite materials*. Dec. 1994. [Online]. Available: https://ci.nii.ac.jp/ncid/BA72621266.

[23] M. Domingo-Espin, J. M. P. Forcada, A. A. García-Granada, J. Llumà, S. Borrós, and G. Reyes, “Mechanical property characterization and simulation of fused deposition modeling polycarbonate parts,” *Materials Design*, vol. 83, pp. 670–677, Oct. 2015. DOI: 10.1016/j.matdes.2015.06.074. [Online]. Available: https://doi.org/10.1016/j.matdes.2015.06.074.

[24] S. Jiang, M. Sun, Y. Zhan, H. Li, and W. Sun, “A dynamic model of laminated material extrusion additive manufacturing plate with the property of orthogonal anisotropy,” *Rapid Prototyping Journal*, vol. 27, no. 4, pp. 785–796, May 2021. DOI: 10.1108/rpj-04-2020-0075. [Online]. Available: https://doi.org/10.1108/rpj-04-2020-0075.

[25] A. Shabana, *Vibration of Discrete and Continuous Systems*. Springer, Oct. 2019.

[26] S. S. Rao, *Vibration of Continuous Systems*. John Wiley Sons, Feb. 2007.

[27] S. Miroslav, *Torsion*, 2014. [Online]. Available: https://structural-analyser.com/domains/SteelDesign/Torsion/.

[28] Domingo-EspinMiquel, BorrosSalvador, AgulloNuria, Garcia-GranadaAndres-Amador, and ReyesGuillermo, “Influence of Building Parameters on the Dynamic Mechanical Properties of Polycarbonate Fused Deposition Modeling Parts,” *3D printing and additive manufacturing*, vol. 1, no. 2, pp. 70–77, Jun. 2014. DOI: 10.1089/3dp.2013.0007. [Online]. Available: https://doi.org/10.1089/3dp.2013.0007.

[29] specialchem, *Density of plastics: Technical properties*, 2024. [Online]. Available: https://omnexus.specialchem.com/polymer-property/density.

[30] *Model 352C22 | PCB Piezotronics*. [Online]. Available: https://www.pcb.com/products?m=352C22.

[31] T. J. Menna, *ASM Handbook*. ASM Internatial, Jan. 2022, vol. 11B. [Online]. Available: https://dl.asminternational.org/handbooks/edited-volume/171/chapter/3730207/Viscoelasticity-of-Plastics.

[32] Esun, *PETG-Filament Technical Datasheet*, Nov. 2021. [Online]. Available: https://3d.nice-cdn.com/upload/file/eSUN_PETG-Filament_TDS_V4.0.pdf.

[33] polyservice kunsthars technieken, *Technische Informatiebladen*, Apr. 2022. [Online]. Available: https://www.polyservice.nl/content/25-technische-informatiebladen.

[34] E. Loukogeorgaki, C. Michailides, and D. C. Angelides, "Hydroelastic analysis of a flexible mat-shaped floating breakwater under oblique wave action," *Journal of Fluids and Structures*, vol. 31, pp. 103–124, May 2012. DOI: 10.1016/j.jfluidstructs.2012.02.011. [Online]. Available: https://doi.org/10.1016/j.jfluidstructs.2012.02.011.

[35] M. Katsouros, "Experimental Investigation of Wet-Deck Slamming on Fully Elastic Catamaran Model," Tech. Rep., Sep. 2024. [Online]. Available: https://repository.tudelft.nl/record/uuid:02f8ee6f-6f0e-4fab-a4bf-4d56e3156889.

A

Planning

	Naam	Duur	Begin	Einde
1	⊟ **deadlines**	136 dagen?	**26-1-24 8:00**	**5-8-24 8:00**
2	submit plan of appraoch for fe	0 dagen	26-1-24 8:00	26-1-24 8:00
3	submit plan of approach	0 dagen	27-1-24 8:00	29-1-24 17:00
4	vibration experiment kick off	0 dagen	30-1-24 8:00	30-1-24 8:00
5	kick off meeting	0 dagen?	5-2-24 8:00	5-2-24 8:00
6	determination of final elastic m	0 dagen	19-2-24 8:00	19-2-24 8:00
7	Greenlight meeting	0 dagen	1-7-24 7:00	1-7-24 8:00
8	final presentation and gradua	0 dagen	5-8-24 7:00	5-8-24 8:00
9	⊟ **experience with experimen**	19 dagen	**30-1-24 8:00**	**23-2-24 17:00**
10	intial meeting	1 dag	30-1-24 8:00	30-1-24 17:00
11	conduction of experiments	15 dagen	5-2-24 8:00	23-2-24 17:00
12	data analysis	3 dagen	21-2-24 8:00	23-2-24 17:00
13	⊟ **material value experiment**	26 dagen	**26-2-24 8:00**	**1-4-24 17:00**
14	study experimental procedure	5 dagen	26-2-24 8:00	1-3-24 17:00
15	design/print samples	5 dagen	4-3-24 8:00	8-3-24 17:00
16	feedback	1 dag	11-3-24 8:00	11-3-24 17:00
17	experiments	10 dagen	12-3-24 8:00	25-3-24 17:00
18	data analysis	5 dagen	26-3-24 8:00	1-4-24 17:00
19	⊟ **create ansys model**	54 dagen	**2-4-24 8:00**	**14-6-24 17:00**
20	create geometrie* maybe unn	20 dagen	2-4-24 8:00	29-4-24 17:00
21	find model for material values	5 dagen	30-4-24 8:00	6-5-24 17:00
22	determine eigenfrequencies/v	2 dagen	7-5-24 8:00	8-5-24 17:00
23	⊟ **validation experiments**	12 dagen	**9-5-24 8:00**	**24-5-24 17:00**
24	establish experimental proce	5 dagen	9-5-24 8:00	15-5-24 17:00
25	experiments	5 dagen	16-5-24 8:00	22-5-24 17:00
26	data analysis	2 dagen	23-5-24 8:00	24-5-24 17:00
27	⊟ **compare with different m**	15 dagen	**27-5-24 8:00**	**14-6-24 17:00**
28	isotropic material	5 dagen	27-5-24 8:00	31-5-24 17:00
29	no strain rate hardening	5 dagen	3-6-24 8:00	7-6-24 17:00
30	no viscous component	5 dagen	10-6-24 8:00	14-6-24 17:00
31	⊟ **writing of report**	116 dagen?	**26-2-24 8:00**	**5-8-24 17:00**
32	begin writing report	116 dagen?	26-2-24 8:00	5-8-24 17:00
33	writing paper	26 dagen?	1-7-24 7:00	5-8-24 17:00
34	writing presentation.	26 dagen	1-7-24 7:00	5-8-24 17:00

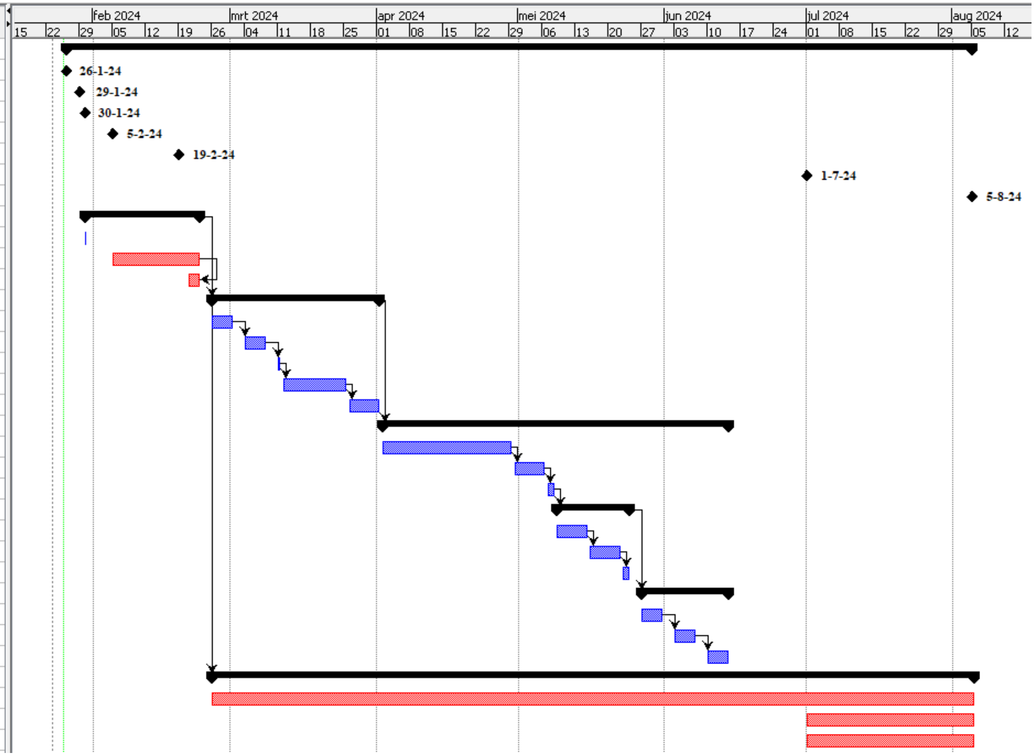

Figure A.1: Planning of project

B

Codes used

B.1. Example ANSYS code

```
finish
/CLEAR
beam_count = 3

!gerenal u-beam dimensions
L_beam = 0.200505797
B_beam = 0.01041575
H_beam = 0.01041575
Thickness_beam = 0.00085775

youngsmodulus = 950000000.0
nu = 0.3
/output,T_shear001,out

meshsize = 0.001
/prep7

mp,dens,1,1073
mp,ex,1,youngsmodulus
mp,prxy,1,nu

*DO,n,0,beam_count,1
k,1+4*n,L_beam*n,B_beam/2,H_beam
k,2+4*n,L_beam*n,B_beam/2,0
k,3+4*n,L_beam*n,-B_beam/2,0
k,4+4*n,L_beam*n,-B_beam/2,H_beam
*ENDDO

!adding outside walls
*DO,m,0,beam_count-1,1
A,1+4*m,4+4*m,8+4*m,5+4*m
A,4+4*m,3+4*m,7+4*m,8+4*m
A,3+4*m,2+4*m,6+4*m,7+4*m
*ENDDO

!adding bulkhead between sections.
*DO,m,0,beam_count,1
```

```
a,1+4*m,2+4*m,3+4*m,4+4*m
*ENDDO

ALLSEL
*IF,beam_count,GT,1,THEN
*DO,n,1,beam_count-1,1
Asel,u,loc,x,L_beam*n
*ENDDO
*ENDIF

ET,1,181
secnum,1
sectype,1,shell
secdata,Thickness_beam
SECOFFSET,top

aesize,all,meshsize
amesh,all

Asel,inve

ET,2,181
secnum,2
sectype,2,shell
secdata,Thickness_beam*2

aesize,all,meshsize
amesh,all

mass_sensor = 0.0005
ET,3,mass21 !adding masses of differen sensors to count for testing.
r,3,mass_sensor,mass_sensor,mass_sensor
TYPE,3
REAL,3
e,3713
e,3772
e,3842
e,10541
e,10642
e,17331
e,17400
e,17459

mass_weight_aded = 0.0305
ET,4,mass21 !adding masses of differen sensors to count for testing.
r,4,mass_weight_aded,mass_weight_aded,mass_weight_aded
TYPE,4
REAL,4
e,3652
e,10591
e,17521

allsel

/solu
antype,2
```

```
modopt,lanb,60,0,,
mxpand,60,,,yes
outres,all,all
solve
/out
```

B.2. Python code to produce ANSYS codes

```
# -*- coding: utf-8 -*-
"""
Created on Thu Jun 20 17:34:22 2024

@author: valen
"""

simulation_count = 5
beam_type = 'T'
import numpy as np




APDL_RUNCODE = f"C:\\Users\\valen\\OneDrive\\Bureaublad\\ansys text files\\APDL_RUNCODE_{beam_type}.

L_beam = 0.200505797*np.ones(simulation_count)#np.random.normal(0.605/3,0.04082/3,simulation_count)
B_beam = 0.010515103*np.ones(simulation_count)#np.random.normal(0.0103222,0.00007857,simulation_coun
H_beam = 0.010515103*np.ones(simulation_count)#np.random.normal(0.0103222,0.00007857,simulation_coun
Thickness_beam = 0.00085775*np.ones(simulation_count)#np.random.normal(0.00076875,0.000021176,simula
youngsmodulus = np.linspace(8e8,1.4e9,simulation_count) #np.random.normal(1.025e9,1e7,simulation_cou
nu = 0.3*np.ones(simulation_count)#np.random.normal(0.3887,0.04,simulation_count)

for n in range(0,simulation_count,1):
    file_path = "C:\\Users\\valen\\OneDrive\\Bureaublad\\ansys text files\\"+beam_type+f"{n:03d}.txt
    with open(file_path, 'w') as APDL_code:
        APDL_code.write("finish\n/CLEAR\nbeam_count = 3\n\n!gerenal u-beam dimensions\nL_beam = "+st
                        "\nB_beam = "+str(B_beam[n])+
                        "\nH_beam = "+str(H_beam[n])+
                        "\nThickness_beam = "+str(Thickness_beam[n])+
                        "\n\nyoungsmodulus = "+str(youngsmodulus[n])+
                        "\nnu = "+str(nu[n])+"\n/output,"+beam_type+f"{n:03d},out\n")
        print(f"File created successfully at: {file_path}")
    with open(APDL_RUNCODE,'r') as runcode:
        runcode_content= runcode.read()
        with open(file_path, 'a') as file:
            file.write("\n"+runcode_content)
output = '/clear\n'
for n in range(0,simulation_count,1):
    output = output+"*use,"+beam_type+f"{n:03d}.txt\nfinish\n"

with open(r'C:\Users\valen\OneDrive\Bureaublad\ansys text files\get.txt','w') as get_code:
    get_code.write(output)
    print('get file created')

#%%

frequency_count = 60
```

```
data_array = np.zeros([frequency_count,simulation_count])

for n in range(0,simulation_count):
    linenum = 0
    data = open(rf"C:\Users\valen\OneDrive\Bureaublad\ansys text files\{beam_type}{n:03d}.out")
    data_frequencies = data.readlines()
    for line in data_frequencies :
        linenum +=1
        if line.find('  MODE    FREQUENCY (HERTZ)      ')>=0:
            break
    print(linenum)
    ANSYS_CALCULATED_FREQUENCIES=data_frequencies[linenum+2:linenum+2+frequency_count]
    for m in range(0,frequency_count):
        data_array[m,n]=ANSYS_CALCULATED_FREQUENCIES[m].split()[1]
data_array = np.matrix.transpose(np.round(data_array,2))
```

C

Determined Youngs modulus for each point

Table C.1: Resulting elastic moduli from shaker testing

Bending	L	Sigma	T	Sigma	V	Sigma
2b	1.74E+09	2.89E+08	1.82E+09	2.18E+08	1.29E+09	3.85E+08
3b	1.55E+09	1.32E+08	1.50E+09	1.22E+08	1.46E+09	1.47E+08
4b	1.41E+09	1.44E+08	1.23E+09	7.91E+07	1.21E+09	2.79E+08
5b	1.35E+09	3.79E+08	1.15E+09	3.42E+08	1.12E+09	2.25E+08
Torsion						
1t	7.00E+08	5.43E+08	3.51E+08	2.96E+08	3.80E+08	3.63E+07
2t	8.00E+08	7.82E+07	5.50E+08	1.38E+08	4.70E+08	1.02E+08
3t	7.79E+08	1.06E+08	4.69E+08	1.08E+08	3.90E+08	8.35E+07
4t	5.60E+08	3.93E+07				